SANDIA REPORT
SAND2006-7579
Unlimited Release
Printed January 2007

Final Report for the ASC Gas-Powder Two-Phase Flow Modeling Project AD2006-09

W. S. Winters and G. H. Evans
Thermal/Fluid Science & Engineering

Prepared by
Sandia National Laboratories
Albuquerque, New Mexico 87185 and Livermore, California 94550

Sandia is a multiprogram laboratory operated by Sandia Corporation,
a Lockheed Martin Company, for the United States Department of Energy's
National Nuclear Security Administration under Contract DE-AC04-94AL85000.

Sandia National Laboratories

Issued by Sandia National Laboratories, operated for the United States Department of Energy by Sandia Corporation.

Available to DOE and DOE contractors from
U.S. Department of Energy
Office of Scientific and Technical Information
P.O. Box 62
Oak Ridge, TN 37831

Telephone: (865) 576-8401
Facsimile: (865) 576-5728
E-Mail: reports@adonis.osti.gov
Online ordering: http://www.osti.gov/bridge

Available to the public from
U.S. Department of Commerce
National Technical Information Service
5285 Port Royal Rd.
Springfield, VA 22161

Telephone: (800) 553-6847
Facsimile: (703) 605-6900
E-Mail: orders@ntis.fedworld.gov
Online order: http://www.ntis.gov/help/ordermethods.asp?loc=7-4-0#online

SAND2006-7579
Unlimited Release
Printed January 2007

Final Report for the ASC Gas-Powder Two-Phase Flow Modeling Project AD2006-09

W. S. Winters and G. H. Evans
Thermal/Fluid Science and Engineering
Sandia National Laboratories
P.O. Box 5800
Livermore, California 94551-0969

Abstract

This report documents activities performed in FY2006 under the "Gas-Powder Two-Phase Flow Modeling Project," ASC project AD2006-09. Sandia has a need to understand phenomena related to the transport of powders in systems. This report documents a modeling strategy inspired by powder transport experiments conducted at Sandia in 2002. A baseline gas-powder two-phase flow model, developed under a companion PEM project and implemented into the Sierra code FUEGO, is presented and discussed here. This report also documents a number of computational tests that were conducted to evaluate the accuracy and robustness of the new model. Although considerable progress was made in implementing the complex two-phase flow model, this project has identified two important areas that need further attention. These include the need to compute robust compressible flow solutions for Mach numbers exceeding 0.35 and the need to improve conservation of mass for the powder phase. Recommendations for future work in the area of gas-powder two-phase flow are provided.

ACKNOWLEDGMENTS

The authors would like to acknowledge the support of the Sierra code development team including Stefan Domino, 01541 and Greg Wagner, 08757 who implemented the baseline two-phase flow model and provided extensions to compressible flow for FUEGO. Stefan and Greg also developed two test problems (channel evacuation and Laval nozzle flow) that are documented in this report. The authors would also like to acknowledge the contributions of Peter Van Blarigan, 08224 and Dave Zanini, 08125 who collected valuable powder evacuation data some of which is presented and discussed here. Finally, the authors would like to thank our advocate, Artie Ortega, 08243 for his interest, encouragement and guidance.

CONTENTS

FIGURES

TABLES

This Page Intentionally Blank

1. THE POWDER EVACUATION PROCESS

During 2001 and 2002 an experimental team led by Peter Van Blarigan, 8243 conducted a series of powder evacuation experiments. The experiments were conducted for a variety of reasons including the evaluation of sweep gases, powders, and control strategies for powder evacuation. During one set of experiments data was collected for the sole purpose of validating a computational model. The purpose of this chapter is to discuss these model validation experiments and to provide some insight into the powder evacuation process. It is hoped that this insight will motivate an appropriate modeling strategy.

1.1. Description of Powder Evacuation Experiments

A schematic of the experimental apparatus is shown in Figure 1. The apparatus includes a regulated supply of helium gas, a stagnation chamber, an inlet tube, a powder storage vessel and an annular exit tube. The annular exit tube surrounds a portion of the inlet tube and carries evacuated power and carrier gas to its final destination (a one atmosphere containment volume). Prior to each experiment the powder storage vessel (a clear plastic spherical vessel having a 19.05 cm internal diameter) was nearly filled (nominally 1 kg) with powder. At time zero a nearly constant mass flow rate of helium was sent to the stagnation chamber. Gas continued to flow until the powder in the storage vessel was completely evacuated. During each experiment, the following quantities were measured as a function of time:

1. Helium gas flow rate.
2. Pressure in the stagnation chamber
3. Temperature in the stagnation chamber
4. Pressure at two locations in the storage vessel
5. Temperature at two locations in the storage vessel
6. The weight of powder leaving the exit tube

In addition to these transient measurements, the initial mass of powder in the storage vessel was measured before each test.

The temperature and pressure in the stagnation chamber were measured so that the thermodynamic state of the gas entering the powder storage vessel could be determined thereby establishing a well-known boundary condition for future modeling. This state was "extrapolated" from the stagnation conditions since it was not possible to measure the thermodynamic state at the vessel inlet. The extrapolation was performed using TOPAZ (the Sandia one-dimensional-transient gas transfer code, see, *e.g.* [1]) by modeling the frictional pressure drop and heat transfer in the inlet tube. These calculations are discussed in subsequent sections.

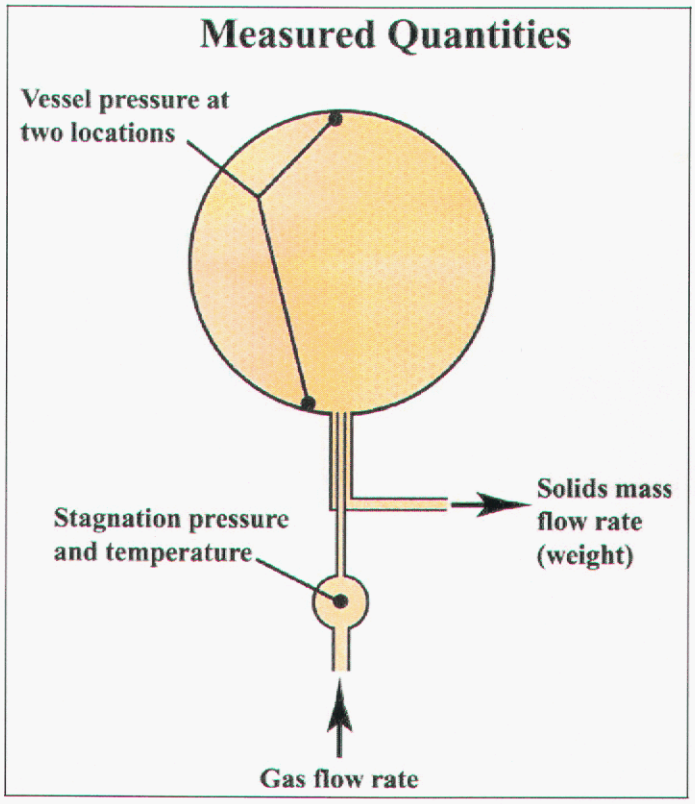

Figure 1. Schematic of experimental apparatus

Pressures and temperatures at two locations in the storage vessel were measured so that modelers could determine if significant spatial pressure/temperature variations occurred during evacuation.

The powder inventory in the storage vessel was determined as a function of time from the initial powder mass measurement and the transient powder weight measurements made downstream of the exit. The measurement assumes the transport time through the exit tube is negligible compared to the time scale for total evacuation. This appears to be a reasonable assumption for all tests discussed here.

Important geometry information for the model validation experiments is summarized as follows:

- Storage vessel ID = 19.05E-2 m
- Inlet tube ID = 4.572E-4 m
- Inlet tube length = 0.1397 m
- Inlet tube extension into vessel = .0127 m
- Exit tube minor ID = 7.874E-4 m
- Exit tube major ID = 17.526E-4 m
- Exit tube length = 5.08E-2 m

Six model validation experiments were performed. These are summarized in Table 1. In the first three experiments the inlet/exit ports for the storage vessel were positioned at the bottom. For the last three the inlet/exit ports were positioned at the top. In all cases the inlet/exit ports were aligned with the centerline of the storage vessel (*i.e.*, the ports were on axis). Three helium gas mass flow rates were tested for each orientation. All experiments were conducted at room temperature.

Table 1. Summary of six powder evacuation experiments.

Nominal Gas Flow Rate - kg/s	Inlet/Exit Position	80% Empty Time - s	Test Number	Initial Powder Mass - Kg
1.44E-04	Bottom	119.6	14	0.975
2.88E-04	Bottom	94.2	11	0.94
4.74E-04	Bottom	72.8	12	0.94
1.50E-04	Top	585.9	19	1.003
3.40E-04	Top	404.8	16	0.971
4.70E-04	Top	491.9	18	0.989

1.1.1. Powder Properties

The powder used in the model validation experiments was Scotchlite glass bubbles H50/10,000 EPX. It is a product commonly used to enhance the coating characteristics of latex house paint. When poured into a drinking glass, one might mistake the powder for milk when viewed from a distance. Despite its "liquid" appearance, it is in fact a powder composed of tiny spheres varying in diameter from 10 to 100 microns. The distribution of particle diameters is shown in Figure 2. It can be seen that approximately 50% of a typical sample volume will pass through a 30 micron filter.

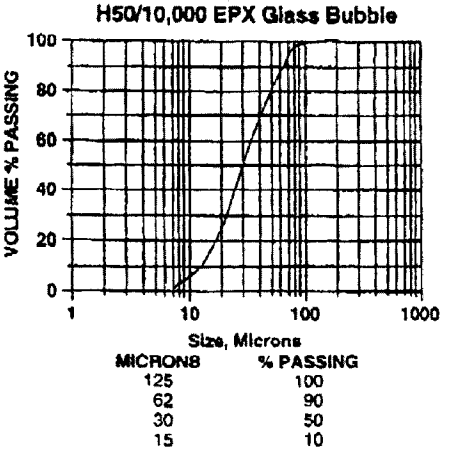

Figure 2. Distribution of powder particle diameters.

Additional physical properties of the powder are:

- Intrinsic density = 500 kg/m^3
- Thermal conductivity = .02 W/m-K
- Specific heat (based on glass) = 837.2 J/kg-K

1.1.2. Gas Properties

The gas used in all powder evacuation experiments was helium. The most non ideal states for helium encountered in the experiments occur in the stagnation vessel where the pressures may reach 7 MPa. According to the N.I.S.T. Reference Fluid Thermodynamic and Transport Properties Database (REFPROP) (see *e.g.*, [2]), the compressibility factor for He at that state is less that 1.04. In the powder storage vessel, the focus of most of the modeling, the compressibility factors drop to 1.003. Hence an ideal gas equation state appears to be appropriate for modeling purposes.

1.2. Summary of Experimental Results

In this section we will begin by discussing experimental results for the bottom inlet/outlet configuration. Next we will discuss results for the top inlet/outlet configuration. We will conclude by discussing features that appear to be common to all tests regardless of inlet/outlet orientation or helium gas flow rate.

Figure 3 shows the storage vessel powder inventory as a function of time for the bottom inlet/outlet configuration. All three helium gas flow rates are represented. The corresponding vessel pressures are shown in Figure 4. Regardless of gas flow rate, the powder evacuation process appears to take place over two fairly distinct time domains. In the first domain a relatively rapid powder evacuation takes place until approximately 80 percent of the powder is purged. Observations through the clear walls of the storage vessel reveal that the bulk of the powder is concentrated in the lower portion of the vessel. One can see the level of highly concentrated powder drop with time until it reaches the bottom where the inlet/outlet tubes are located. When the level reaches the bottom, the powder evacuation process enters a second time domain in which most of the remaining powder in the vessel is entrained in a swirling and relatively dispersed two phase flow. Evacuation during the second time domain is significantly slower as indicated by the "knee" in the powder evacuation curves of Figure 3. Although most of the powder evacuation occurs in the first time domain, most of the time required to do a complete evacuation occurs in the second.

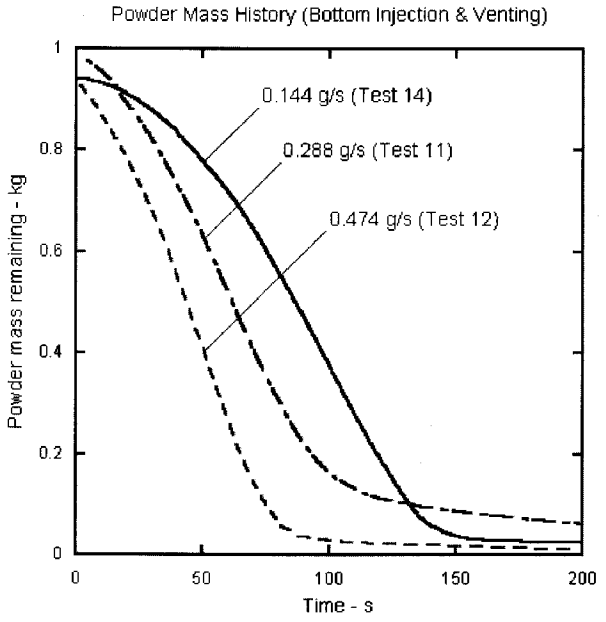

Figure 3. Powder mass inventory for bottom inlet/outlet.

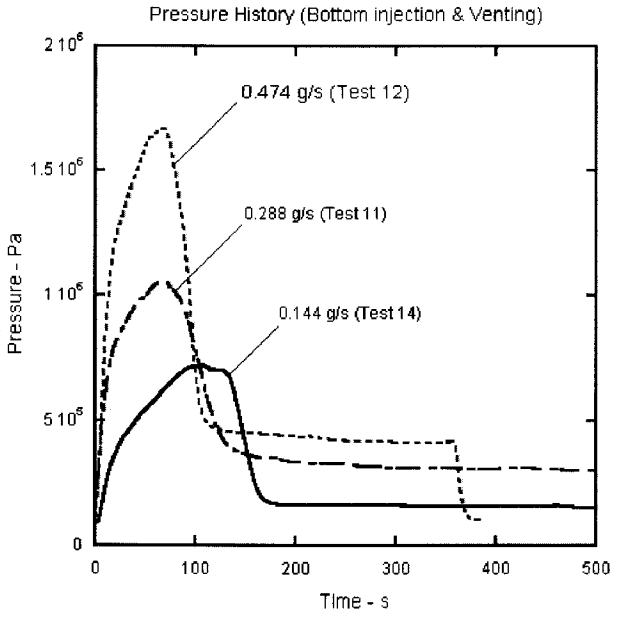

Figure 4. Vessel pressure histories for bottom inlet/outlet.

The powder evacuation curves in Figure 3 appear to be "geometrically similar." If each test had begun with the same mass of powder in the vessel, one might expect the intermediate flow rate curve (green curve, 0.288 g/s helium gas flow rate) to lie between the low and high rate curves over the first 100 seconds of the test. It is interesting to note that for the intermediate flow rate test the "knee in the curve" occurs with more powder remaining in the vessel suggesting that for some reason this gas flow rate is capable of entraining more powder. The time required to purge 80% of the powder is plotted as a function of helium flow rate in Figure 5. Eighty percent purge times appear to be nearly linear with helium flow rate. A least squares linear fit is also shown in Figure 5.

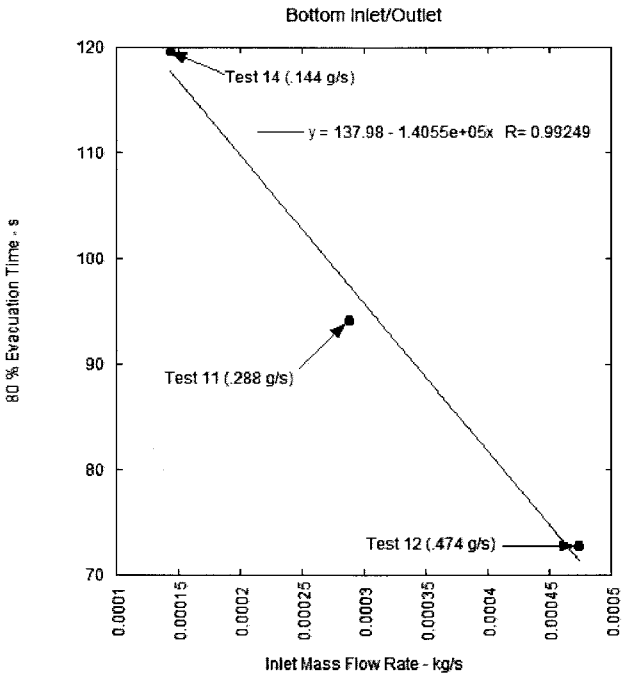

Figure 5. Influence of helium gas flow rate on powder 80% evacuation time (bottom inlet/outlet).

The pressure transients shown in Figure 4 indicate that the pressure rises rapidly during the first part of the transient when 80% of the powder is purged. The pressure then decays to lower level before finally approaching a steady state value. The steady state value is the pressure level in the vessel after all powder is purged. As one might expect, higher steady state pressure levels are associated with higher gas mass flow rates.

Figure 6 shows the storage vessel powder inventory as a function of time for the top inlet/outlet configuration. All three helium gas flow rates are represented. The corresponding vessel pressures are shown in Figure 7. As shown in Figure 6, powder evacuation times are significantly longer than those observed for bottom inlet/outlet. Furthermore, the previously observed time domains for powder evacuation are less distinct; the location of the "knee" in the curve is not as obvious.

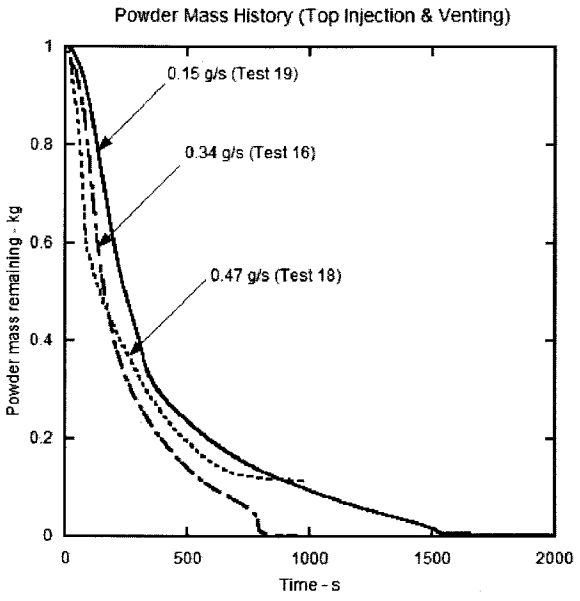

Figure 6. Powder mass inventory for top inlet/outlet.

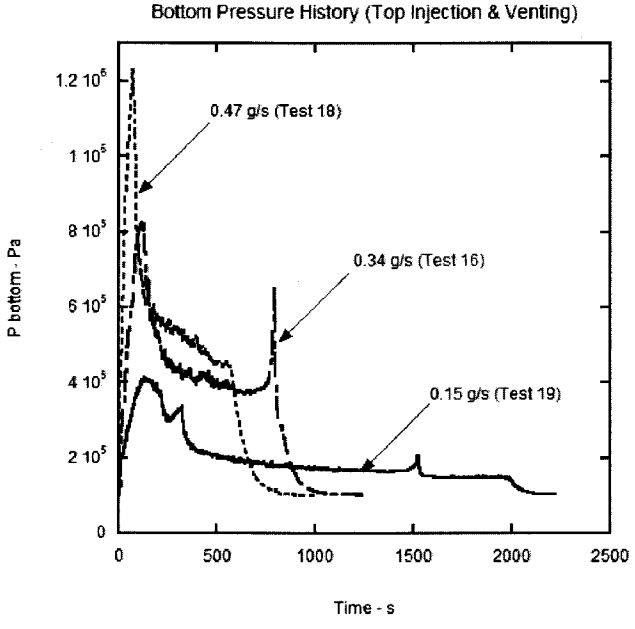

Figure 7. Vessel pressure histories for top inlet/outlet.

The previously observed trend that higher helium gas flow rates lead to more rapid powder evacuation appears to be only partially true for the top inlet/outlet configuration. Figure 8 shows 80% purge times for the three helium flow rates. Increasing the helium gas flow rate from .150 g/s to .340 g/s decreases the 80% evacuation time by approximately 180 seconds. But a further increase in flow rate to .470 g/s actually increases the 80% evacuation time. The powder evacuation curves shown in Figure 6 shows that the .470 g/s flow rate is "on track" to produce a more rapid evacuation but something occurs at 200 seconds to cause the evacuation rate to decrease. The .470 g/s curve crosses the .340 g/s and the rate of evacuation slows dramatically. It is unclear at this point whether this anomaly is due to an unexpected event during the testing (*e.g.* a temporarily clogged exit tube) or the beginning of repeatable trend in the fluid mechanics.

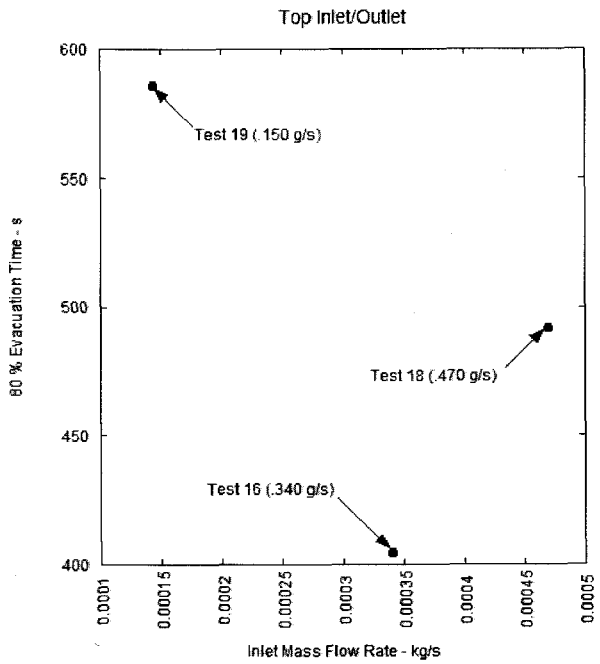

Figure 8. Influence of helium gas flow rate on powder 80% evacuation time (top inlet/outlet).

A number of experimental observations appear to be consistent for all tests regardless of helium gas flow rate or inlet/outlet orientation. Figure 9 shows the measured transient pressure at two locations in the powder storage vessel (Test 12). The pressures at the top and bottom of the vessel appear to be nearly identical for the entire duration of the test. Since this was observed for all tests, it seems reasonable to conclude that the pressure distribution in the vessel is spatially uniform, but time varying, for the entire powder evacuation process.

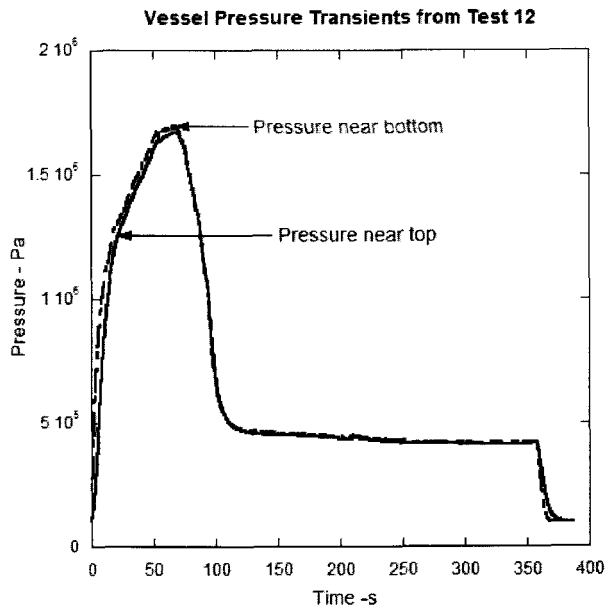

Figure 9. Measured pressure at two locations in the vessel (Test 12).

Figure 10 shows the measured transient temperature at two locations in the vessel (Test 12). The two transients appear to track each other although small temperature differences are apparent. The entire temperature excursion in the vessel over time is approximately 10 K. Similar temperature excursions and distributions were observed for all tests suggesting that modeling the process as isothermal might be a reasonable approach.

Although the intent was to provide constant helium gas flow rates for each test, some variations over time were unavoidable. Figure 11 shows the measured helium gas flow rate during Test 12. Although the nominal helium mass flow rate is quoted as .474 g/s, flow rates reach nearly .5 g/s near the end of the test. Similar mass flow variations were observed for the other tests.

Time variations in measured temperatures and pressure in the stagnation vessel upstream of the inlet tube were also observed. Figure 12 shows these variations for Test 12.

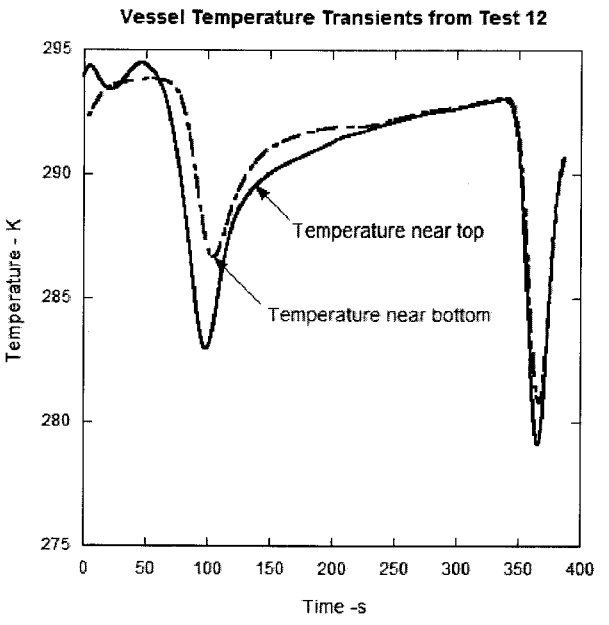

Figure 10. Measured temperature at two locations in the vessel (Test 12).

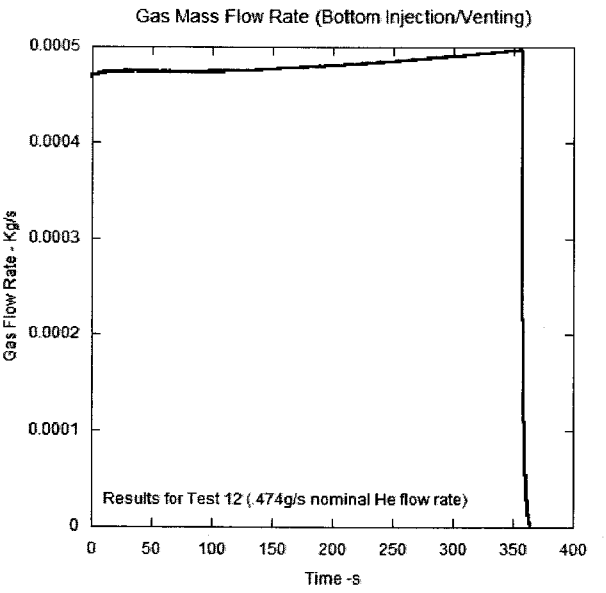

Figure 11. Measured helium gas flow rate for Test 12.

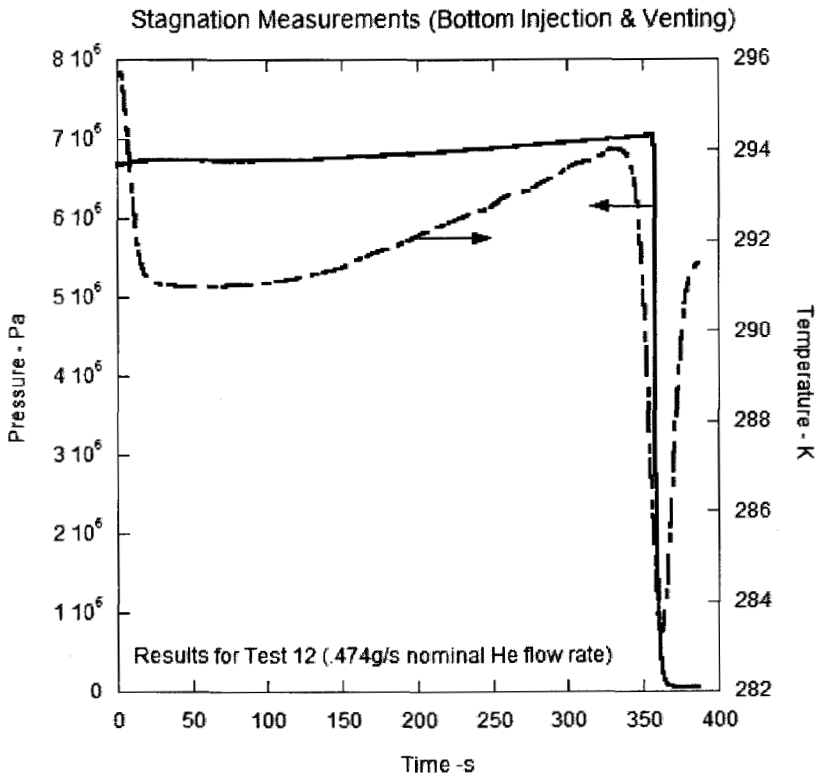

Figure 12. Measured stagnation temperature and pressure for Test 12.

1.3. Compressibility Effects

An important factor in understanding the powder evacuation process is the compressibility of the entrainment gas (helium). The experimental data suggests that compressibility is important, at least for some aspects of the problem. Consider, for example, Figure 13, which shows the measured pressure and computed mass of helium in the vessel as a function of time for Test 12. The helium mass curve was computed from the experimental data using the following relationship:

$$M_g(t) = P_g(t)\left(V_{vessel} - M_s(t)/\rho_s\right)/RT \qquad (1.1)$$

Where $M_g(t)$ is the computed mass of gas in the vessel, $P_g(t)$ is the measured pressure in the vessel, V_{vessel} is the vessel volume, $M_s(t)$ is the measured powder mass in the vessel, ρ_s is the density of the solids, R is the ideal gas constant for helium, and T is the nominal temperature in the vessel (293 K).
Figure 13 shows that peak helium mass in the vessel occurs at a time when the vessel is partially filled with solids. If the helium was modeled as being incompressible, the

peak gas mass would occur at the end of the process when the vessel contains only gas; *i.e.*, one would expect the mass to increase monotonically from time zero to the time when all solids are purged. Clearly if predicting gas utilization and peak vessel pressure (*i.e.*, safety margins) is important, compressibility of the carrier gas must be considered.

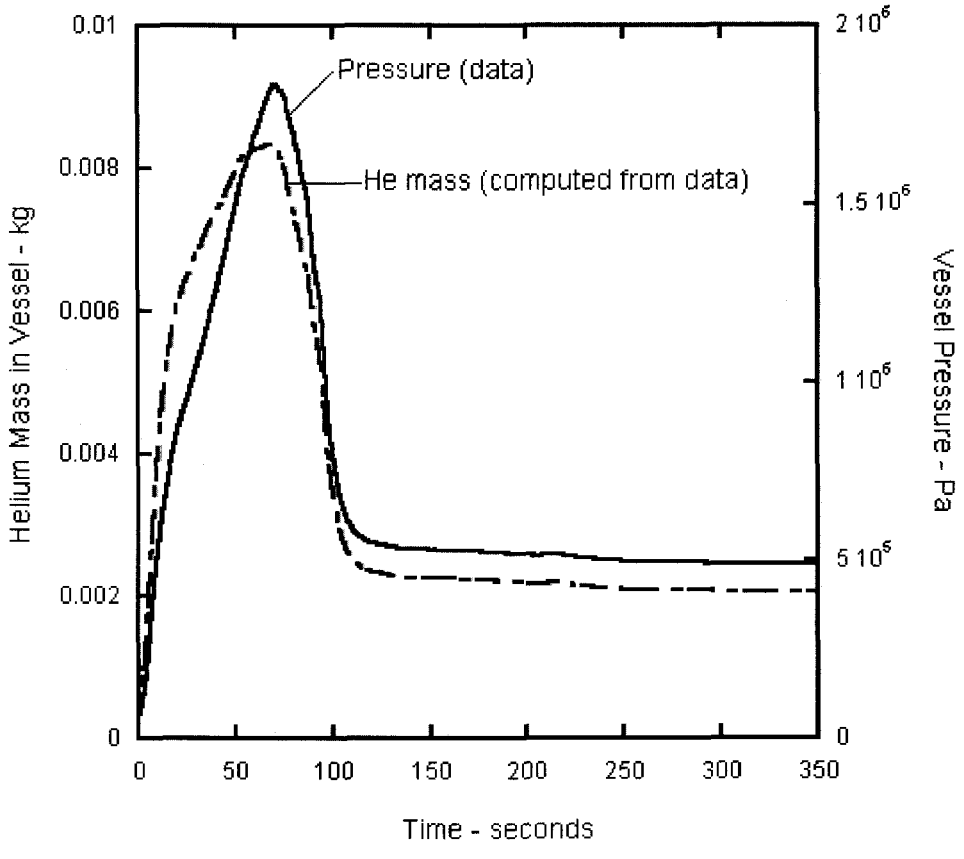

Figure 13. Measured pressure and computed mass of helium in vessel (Test 12).

1.4. TOPAZ Modeling

A TOPAZ simulation of the stagnation vessel, inlet tube, powder storage vessel, outlet tube and ambient was developed to model the single phase helium gas flow. A schematic of the modeled system is shown in the upper part of Figure 14. The lower part of Figure 14 shows the TOPAZ model using symbols familiar to TOPAZ modelers (see *e.g.*, Reference [3]). TOPAZ treats all vessels as single control volumes in which perfect mixing occurs. Tubes are modeled as a string of linked control volumes that represent a one-dimensional transient finite difference representation of the compressible flow conservation equations (continuity, species, momentum and energy). Multidimensional

effects such as tube wall heat transfer and frictional pressure drop are accounted for using locally applied quasi-steady correlations.

Under steady state conditions the model of Figure 14 predicts pressure levels and flow rate for the end of the powder evacuation problem when the powder is fully evacuated. More importantly, the model can be used as a tool to determine the state of the helium gas as it enters the power storage vessel for the entire process. This boundary condition information is needed to properly formulate the two phase flow problem.

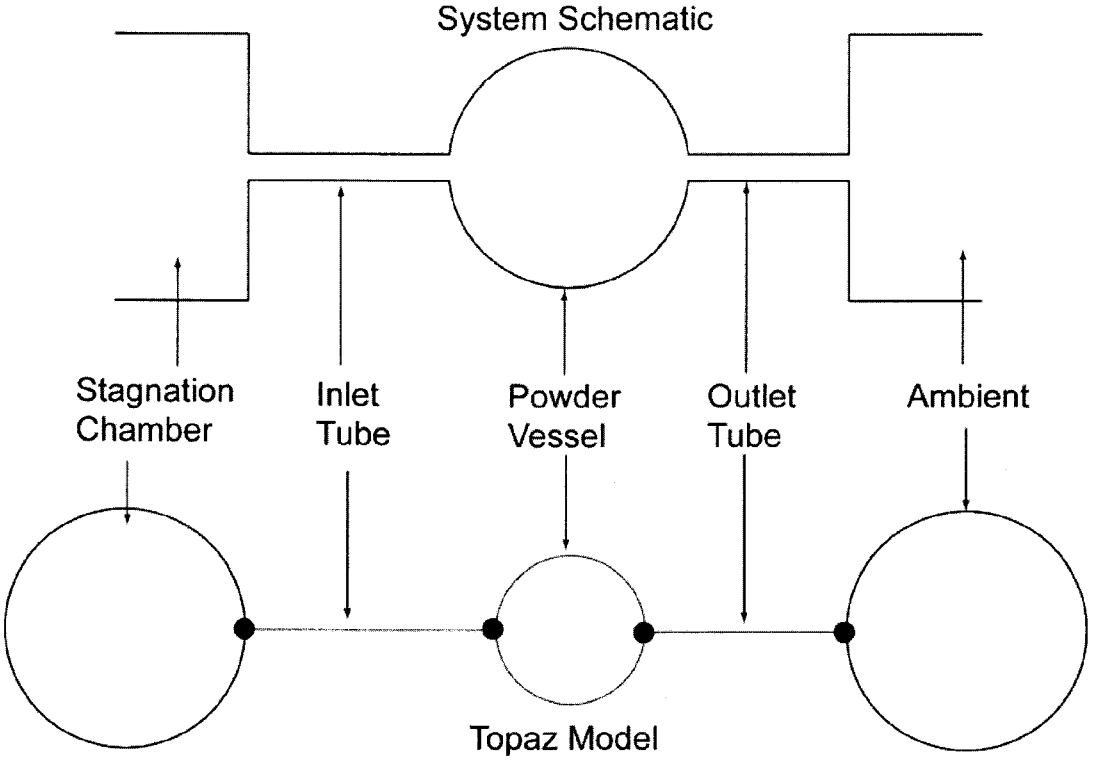

Figure 14. TOPAZ model for helium gas flow.

In the TOPAZ simulation the stagnation vessel was modeled as an infinitely large reservoir capable of supplying helium at the measured stagnation pressure and temperature. Although these measured values varied slightly with time, the TOPAZ model treats them as constants. The ambient was also modeled as an "infinite vessel."

Pressure drop in the inlet tube was modeled using the default Moody pipe friction model. The default model assumes that the tube wall is hydraulically smooth. The annular exit tube was modeled as a 2 inch (.0508 m) long tube having a cross sectional flow area of the annulus and an appropriate hydraulic diameter. Using the default frictional pressure drop model for the exit tube caused the TOPAZ model to under predict pressure levels in the powder vessel. For this reason a constant "tuned" friction factor was used for the exit tube. The friction factor value was selected so that the predicted vessel pressure level for the end of Test 12 matched the measured value. The friction factor fitted from Test 12

was then used to simulate all tests and represents the only empirically fitted parameter in the TOPAZ model.

Results from the TOPAZ modeling are summarized in Table 2. Using the measured values for total temperature and pressure in the stagnation vessel, TOPAZ was able to predict values for helium flow rate which were close to those measured. The poorest agreement occurred for Test 19 (low flow rate, top inlet/outlet); the predicted value was 10.7% less than the measured value. Agreement for the other tests is considerably better. The best agreement occurred for Test 11 (intermediate flow rate, bottom inlet/outlet); the predicted value was only 1.4% higher than the measured value. Some of the differences in predicted and measured values can be attributed to the fact that measured stagnation properties and flow rates actually varied slightly in time. This was not accounted for in the modeling where only average (constant) values for stagnation properties were used.

Table 2. Measured and predicted helium flow parameters from six tests.

Test Number	Measured Gas Flow Rate - kg/s	TOPAZ Predicted gas mass transfer - kg/s	Measured Final Vessel Pressure - Pa	TOPAZ Predicted Vessel Pressure - Pa	TOPAZ Predicted Inlet Mach Number	TOPAZ Predicted Exit Mach Number
14	1.44E-04	1.36E-04	1.50E+05	1.448E+05	1.000E+00	4.130E-01
11	2.88E-04	2.92E-04	3.05E+05	2.65E+05	1.00E+00	8.120E-01
12	4.74E-04	4.63E-04	4.19E+05	4.19E+05	1.00E+00	1.000E+00
19	1.50E-04	1.340E-04	1.50E+05	1.44E+05	1.00E+00	4.071E-01
16	3.40E-04	3.17E-04	3.90E+05	2.86E+05	1.00E+00	8.653E-01
18	4.70E-04	4.41E-04	4.55E+05	3.99E+05	1.00E+00	1.000E+00

As mentioned previously, the only model "tuning" that was done involved the assignment of a friction factor for the annular exit tube. This tuning played no role in the prediction of helium flow rate for the six tests since in all cases choking occurred at the inlet to the powder vessel (see, *e.g.*, the vessel inlet Mach numbers listed in column six of Table 2). In the mass flow prediction, choking (Ma=1) at the vessel inlet eliminates the pressure drop influence of all hardware downstream.

Specification of an exit tube friction factor has more of an impact on the prediction of the powder vessel pressure levels. The poorest agreement between measure and predicted vessel pressure occurred for Test 16 (intermediate flow rate, top inlet/outlet) where the predicted value is 26.6% lower than the measured value. Close examination of Figure 7 shows that Test 16 may have been terminated before a true steady state vessel pressure was achieved. This may have contributed to the poor agreement. The best agreement between measured and predicted vessel pressure levels was for Test 12 since this was the test that was used to select the exit tube friction factor.

Column seven of Table 2 shows TOPAZ predicted Mach numbers for flow leaving the exit tube and entering the ambient space. Predictions show that this flow is highly compressible with Mach numbers ranging from approximately 0.4 up to 1.0 (choked flow). One should keep in mind that these predictions are for pure gas. During powder evacuation, the pressure drop in the exit tube due to the presence of the two phase mixture is likely to be higher and the flow may be unchoked. On the other hand, flow choking for a two phase mixtures may occur at pressure ratios that are quite different than those of the carrier gas.

Few general conclusions regarding the exit flow boundary condition can be drawn from pure gas TOPAZ simulations. However, TOPAZ modeling can be useful in postulating an inflow boundary condition for the powder vessel.

Modeling enables us to extrapolate measured flow rates and stagnation pressures and temperatures to the inlet boundary. The model presented here is capable of predicting the thermodynamic state of the helium up to the point where the Mach number is 1.0, *i.e.* the state entering the powder evacuation vessel. Since the TOPAZ models focus on the steady helium flow at the end of the process, predicted inlet Mach numbers represent the highest values encountered during powder evacuation.

In following sections a method will be proposed to extrapolate the TOPAZ-predicted Ma=1.0 state to a subsonic inlet boundary condition that can be used for modeling the powder evacuation process.

1.5. The Under Expanded Jet

We have demonstrated that Helium enters the powder storage vessel as an under expanded jet. Flow is sonic or Mach 1 at or near the inlet and expands supersonically to a shock structure that sonically insulates the inlet from the two phase flow in the vessel. The location of the shock structure and its size will depend on the downstream pressure (vessel pressure) but the mass flow rate of helium will not. Furthermore no powder can travel upstream through the shock structure.

Figure 15 shows the "typical" shock structure for an under expanded jet. The figure is reproduced from reference [4]. The main feature of the shock structure is a Mach disk or shock D_m in diameter and a distance X_m from the inlet. In addition there are expansion fans and an intercepting shock structure at the jet boundaries adjacent to the jet. Flow expanding from the inlet either passes through the single shock represented by the Mach disk or through the series of shocks at the jet boundary.

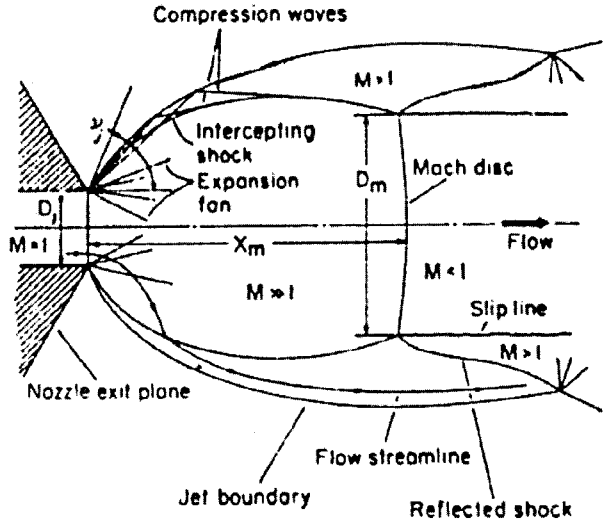

Figure 15. The structure of an under expanded jet (Crist).

A shadowgraph of an actual under expanded jet is shown in Figure 16. The Mach disk and expansion fans at the jet boundary are clearly visible.

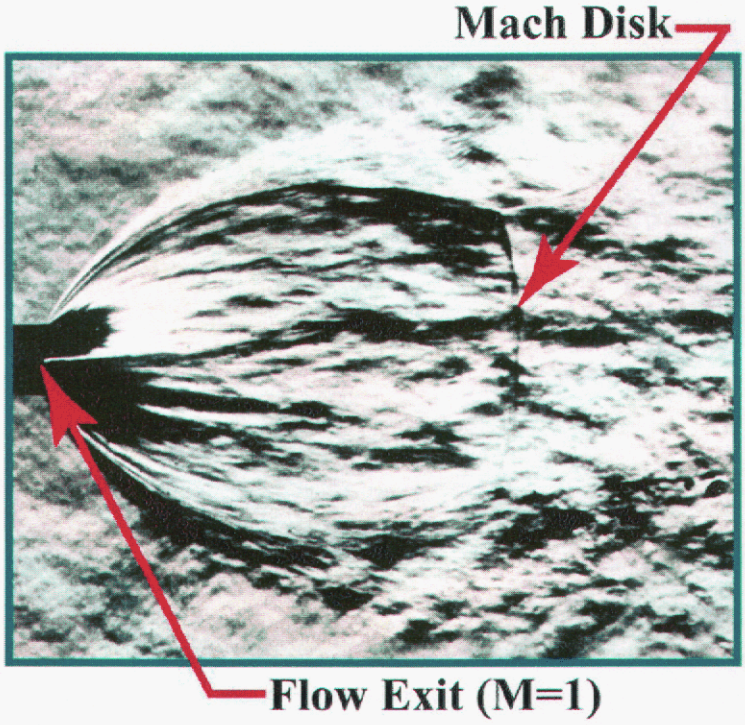

Figure 16. Shadow graph of an under expanded jet.

Crist *et. al.* [4] conducted experiments to characterize the size and location of the Mach disk. Some of their results are presented here in Figures 17 and 18. Figure 17 shows the Mach disk diameter as a function of nozzle pressure ratio P_o / P_∞ (exit stagnation pressure divided by downstream or vessel pressure). The abscissa is the Mach disk diameter, D_m normalized by the nozzle exit diameter, D_j. Figure 18 shows the Mach disk location, X_m, as a function of the nozzle pressure ratio where X_m is the distance between the nozzle outlet plane and the position of the Mach disk. Here again, results are normalized by the nozzle exit diameter.

The nozzle pressure ratio computed by TOPAZ for steady state gas flow in Test 12 is 7.6. This pressure ratio falls below the range investigated by Crist *et. al.* However for a pressure ratio of 10, Crist *et. al.* predict a Mach disk diameter approximately equal to the nozzle exit diameter. Its distance from the nozzle exit is approximately two nozzle exit diameters (see Figure 18).

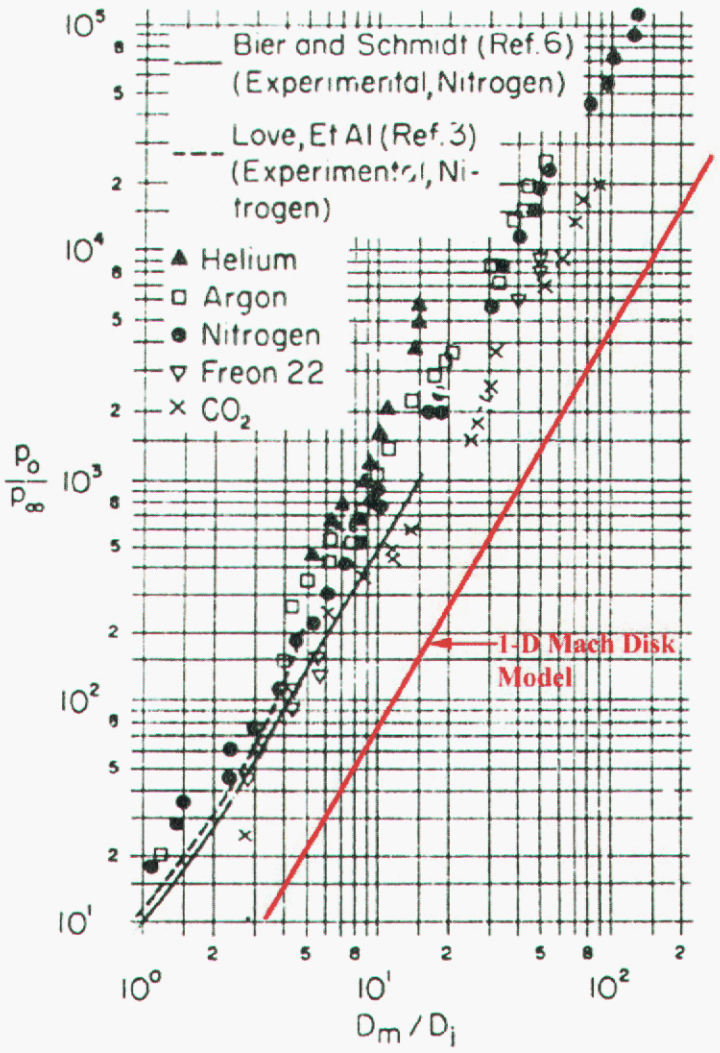

Figure 17. Mach disk diameter as a function of nozzle pressure ratio from [4].

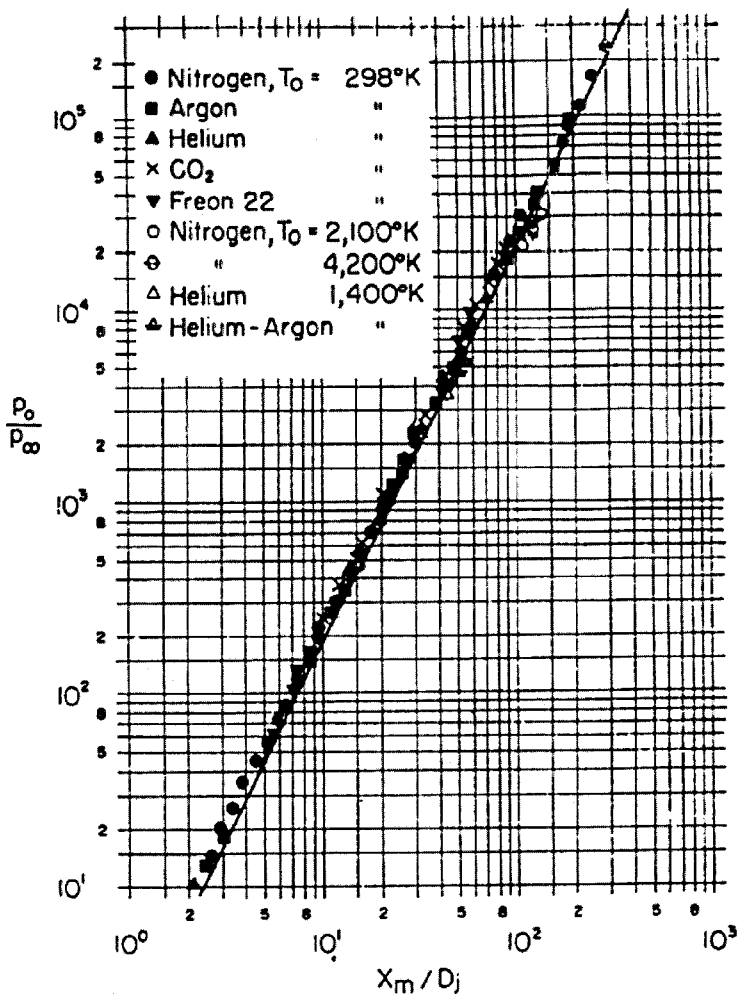

Figure 18. Mach disk location as a function of nozzle pressure ratio from [4].

Addy [5] conducted experiments to characterize the size and location of the Mach disk for nozzle pressure ratios less than 10. His results are reproduced here in Figure 19. The data is presented in the form used by Crist *et. al.* except that abscissa and ordinate has been reversed and the nomenclature is slightly different (L_{md} is the Mach disk position relative to the nozzle exit, D_{md} is the Mach disk diameter and P_b is the downstream or vessel pressure). Curves 1 and 2 and related data show Mach disk diameter for slightly different nozzle shapes and Curve 3 shows Mach disk position. For a pressure ratio of 7.6 Addy's data suggest the Mach disk diameter will be approximately half the nozzle diameter and its position will be approximately 1.7 nozzle diameters from the nozzle exit.

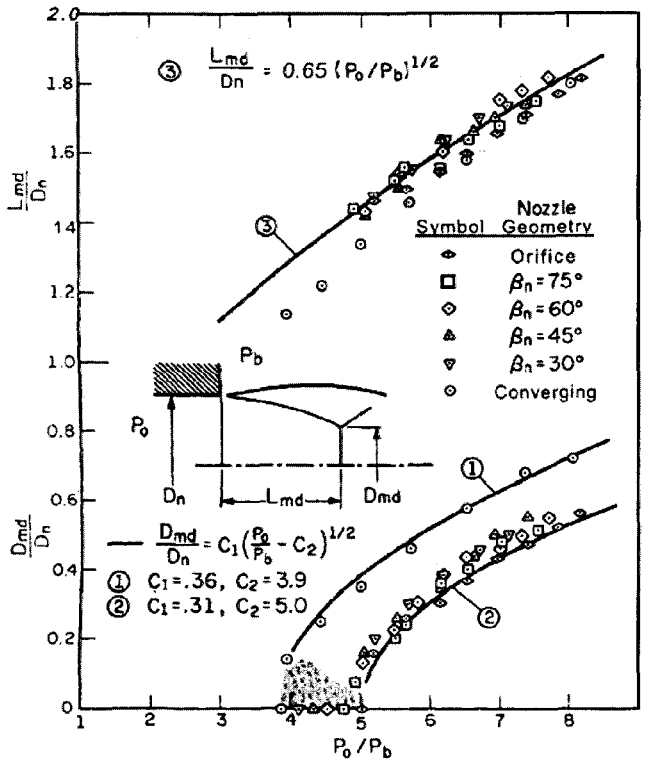

Figure 19. Mach parameters as a function of nozzle pressure ratio from [5].

The experimental observations of Crist *et. al.* [4] and Addy [5] indicate that for the conditions and geometry of the powder evacuation problem, supersonic flow is confined to a very small area close to the inlet. It would appear that formulating an inlet boundary condition that neglects the supersonic nature of incoming gas will have little effect on the two phase flow computations provided the correct gas mass flow rate and principle flow direction is preserved for the incoming helium jet. The next two sections will outline boundary condition treatments that avoid resolving the details of supersonic flow.

1.6. The Single Mach Disk Model

The single Mach disk model is based on an idealization of the incoming flow shown in Figure 20. The model assumes flow of a perfect gas and the development of a planar shock or Mach disk. Gas is assumed to be flowing at a steady mass flow rate $\dot{m}$. Choked flow at the inlet expands isentropically to a location in the vessel where a single Mach disk forms and the flow "shocks" to the vessel pressure. All the flow entering the inlet is assumed to flow through the single Mach disk. The model will determine the size of the Mach disk and the state of the gas at locations 2 and 3. State 2 is the supersonic state just upstream of the Mach disk and State 3 is the subsonic (but still compressible) state downstream of the Mach disk. The model will not predict the position of the Mach disk relative to the inlet but we know from the previous section that for our pressure ratios, this position is extremely close to the inlet.

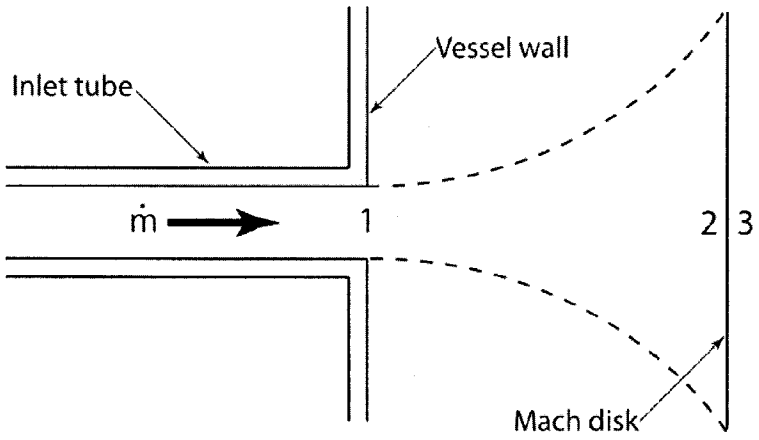

Figure 20. Mach disk model.

State 1 corresponds to the end of the inlet tube where the flow is choked and the Mach number is 1.0. From the measurements made in the upstream stagnation chamber and the TOPAZ extrapolations, everything is known regarding the state of the gas at 1. We could use this information directly as a boundary condition if our CFD code was capable of modeling transonic flows and complicated shock structures. Instead we will utilize the single Mach disk model to design a new subsonic inlet boundary condition. This new boundary condition will have an inlet diameter of the Mach disk and an incoming gas state equivalent to state 3.

From Shapiro [6], page 118, it can be shown that the Mach number, M_2, upstream of the Mach disk (or shock) is related to the pressures P_2 and P_3 by:

$$\frac{P_3}{P_2} = \frac{2\gamma}{\gamma+1} M_2^{\,2} - \frac{\gamma-1}{\gamma+1}. \tag{1.2}$$

Static pressures P_2 and P_3 may be expressed in terms of the corresponding Mach numbers M_2 and M_3, and total pressures P_{02} and P_{03} as:

$$P_2 = P_{02}\left(1+\frac{\gamma-1}{2}M_2^{\,2}\right)^{-\frac{\gamma}{\gamma-1}} \tag{1.3}$$

$$P_3 = P_{03}\left(1+\frac{\gamma-1}{2}M_3^{\,2}\right)^{-\frac{\gamma}{\gamma-1}}. \tag{1.4}$$

Since we have assumed the flow between state 1 and 2 to be isentropic, it follows that

$$P_{02} = P_{01}. \tag{1.5}$$

Shapiro [6], page 118 provides a relationship between the Mach numbers upstream (M_2) and downstream (M_3) of the Mach disk as:

$$M_3^2 = \frac{M_2^2 + \frac{2}{\gamma - 1}}{\frac{2\gamma}{\gamma - 1} M_2^2 - 1}. \tag{1.6}$$

Substituting Equations (1.3) through (1.6) into (1.2) yields the following transcendental algebraic equation for M_2:

$$\frac{P_{03}\left[1 - \frac{\gamma - 1}{2}\left(\frac{M_2^2 + \frac{2}{\gamma - 1}}{\frac{2\gamma}{\gamma - 1} M_2^2 - 1}\right)\right]^{\frac{\gamma}{\gamma - 1}}}{P_{01}\left(1 + \frac{\gamma - 1}{2} M_2^2\right)^{\frac{\gamma}{\gamma - 1}}} = \frac{2\gamma}{\gamma + 1} M_2^2 - \frac{\gamma + 1}{\gamma - 1}.$$

(1.7)

The stagnation pressures P_{03} and P_{01} are known (inlet stagnation pressure and downstream vessel pressure respectively). All that remains is to solve Equation (1.7) for M_2, the Mach number upstream of the Mach disk. In the present study, a simple computer program was developed to accomplish this.

With M_2, known, all properties at states 2 and 3, and the Mach disk diameter may be easily calculated. Recalling that the flow from 1 to 2 is isentropic such that $T_{02} = T_{01}$, it follows that

$$T_2 = T_{01}\left(1 + \frac{\gamma - 1}{2} M_2^2\right)^{-1}.$$

(1.8)

With T_2 determined from Equation (1.8) and P_2 determined from Equation (1.3), the state at 2 is fully specified. The density and sound speed at state 2 are given by

$$\rho_2 = \frac{P_2}{RT_2} \tag{1.9}$$

$$c_2 = \sqrt{\gamma R T_2} \tag{1.10}$$

respectively.

Flow continuity may now be used to determine the Mach disk cross-sectional area and diameter, *i.e.*,

$$A_2 = A_3 = \frac{\dot{m} c_2}{\rho_2 M_2} \tag{1.11}$$

$$D_2 = D_3 = \sqrt{\frac{4A_2}{\pi}}\,. \tag{1.12}$$

Utilizing expressions developed in Shapiro [6], page 117, state 3 may be specified by

$$T_3 = T_2 \left(\frac{1 + \frac{\gamma - 1}{2} M_2^{\,2}}{1 + \frac{\gamma - 1}{2} M_3^{\,2}} \right) \tag{1.13}$$

and

$$P_3 = P_2 \frac{M_2}{M_3} \frac{\sqrt{1 + \frac{\gamma - 1}{2} M_2^{\,2}}}{\sqrt{1 + \frac{\gamma - 1}{2} M_3^{\,2}}}\,. \tag{1.14}$$

This completes the formulation of the Mach disk model. For the conditions at the end of Test 12 (highest He flow rate, inlet/exit at the bottom, vessel nearly void of powder), The Mach disk model gives rise to following:

$$\begin{aligned} D_2 = D_3 &= 0.148 \text{ cm} \\ \dot{m} &= .474 \text{ g/s} \\ M_3 &= .474 \\ T_3 &= 300.3 \text{ K} \end{aligned}$$

The Mach disk model indicates that the original boundary condition consisting of choked helium flow through a .0457 cm ID inlet could be replaced with an equivalent subsonic but compressible (M_3=.474) flow through a 0.148 cm ID inlet at a temperature of 300.3 K.

The simple Mach disk model is attractive since it is physically motivated and provides us with a means to completely define an equivalent subsonic inlet for a choked flow. However, it has two serious disadvantages when applied to the powder evacuation problem. First, the vessel pressure and consequently the Mach disk diameter varies throughout the evacuation transient. Second, the computed Mach disk is considerably larger than those observed in actual experiments. The second point is illustrated in Figure

17. The single Mach disk model was used to calculate Mach disk diameters over a range of the inlet-to-vessel pressure ratios. These results are shown as the red line in Figure 17. Application of the single Mach disk model results in larger computed disk diameters over the entire range of pressure ratios. The larger computed diameters are likely due to the assumption that all flow must pass through the Mach disk. In reality, a portion of the flow will pass through the compression waves at the jet boundary (dashed lines in Figure 20). Hence the actual Mach disk diameter need not be as large as the theoretical value to accommodate the flow.

1.7. An Alternative Subsonic Inlet (ASI) Boundary Condition

A simple subsonic inlet boundary condition may be specified by assuming the prescribed flow rate enters through a larger hole. We will call this the alternative subsonic inlet (ASI) boundary condition. If assumed inlet diameters are large enough, ASI will result in Mach numbers that are less than one. There are some common sense limitations as to how large the inlet diameter can be. We would still like to retain an inlet diameter that is at least two orders of magnitude smaller than the vessel diameter so the incoming flow would look like a point source for flow to an observer some distance away from the inlet. In the Sandia powder evacuation experiments the vessel diameter is 417 times larger that the inlet diameter. Opening the inlet to the previously computed Mach disk diameter of 0.148 cm would result in vessel diameter-to-inlet diameter ratio of 129 still (hopefully) a point source for flow in a large vessel. Clearly, changing the inlet diameter will have some influence on the incoming jet. The underlying assumption for ASI (and for the single Mach disk model) is that such changes will have a negligible effect on the powder evacuation process. In any event, this is an assumption that can be verified computationally by determining if small inlet diameter variations have an influence on predicted evacuation times. It is important to remember that regardless of the assumed inlet diameter, the mass flow rate of incoming gas will be preserved but not necessarily its momentum.

The only remaining uncertainty regarding the ASI is the state of the incoming gas. It is safe to assume that the incoming total temperature of the gas stream remains unchanged regardless of whether the flow is subsonic or choked (see *e.g.* [6]). Since the incoming total temperature (determined from measured stagnation values in the chamber upstream and extrapolated to inlet conditions by TOPAZ) is roughly room temperature and the total temperature in the powder storage vessel (measured in the Sandia Powder evacuation experiments) is also roughly room temperature, it seems reasonable to assume that the incoming gas stream retains the energy content of the gas already in the vessel. If we further assume that the incoming stream takes on the total pressure in the vessel, we have established the state of the incoming flow.

We can summarize the ASI boundary condition as a mass flow rate boundary condition in which the velocity will depend on the assumed inlet diameter and the state of the incoming gas will be identical to the state of the gas in the powder vessel adjacent to the inlet. For the conditions at the end of Test 12 (highest He flow rate, inlet/exit at the bottom, vessel nearly void of powder), and an assumed inlet diameter equal to the previously

computed Mach disk diameter, the ASI gives rise to following:

$$D = 0.148 \text{ cm}$$
$$\dot{m} = .474 \text{ g/s}$$
$$M_3 = .428$$
$$T_3 = 290\text{K}$$

The ASI boundary condition is nearly equivalent to the previously computed single Mach disk treatment. However ASI allows us more flexibility in changing the assumed inlet diameter.

1.8. The Exit Boundary Condition

It would be desirable to assign a total pressure boundary condition equal to one atmosphere across the exit plane in the powder evacuation problem. The exit plane may be selected as either (a) the end of the annular exit tube or (b) a larger flow area downstream of the annular exit tube where the Mach number is certain to be less than one. The measurements and TOPAZ calculations summarized in Table 2 indicate that option (a) is incorrect for the high flow rate test (Test 12) since the flow is choked near the end of the powder transfer. Option (a) is still viable if a boundary condition can be developed that switches between a specified total pressure of one atmosphere and flow limiting boundary condition that restricts the flow of gas to Mach 1. Option (b) is a much simpler boundary condition but the code would be required to compute some kind of shock structure downstream of the annular exit but upstream of the total pressure exit boundary (at least for the end of the high flow rate transfer of Test 12). This would be challenging for a single phase flow. The complexities introduced by having to deal with two-phase flow are unknown.

1.9. Summary

In this chapter we interpret the data obtained from Sandia powder evacuation experiments for the purpose of motivating a modeling strategy. The experiments show that powder evacuation occurs in two stages, a relatively short period of time when most of the powder is evacuated as a dense particle stream and a much longer period of time in which a dispersed field of particles recirculates in the vessel many times before finally exiting. For a bottom inlet/outlet increasing the mass flow rate of the entrainment gas leads to shorter evacuation times. For injection from the bottom of the vessel evacuation times (the first 80% of the evacuation process) decrease linearly with gas flow rate. Injection/exit from the bottom of the vessel produces shorter evacuation times than injection/exit from the top. The data indicates that in order to model the powder evacuation the compressibility (variation of density with pressure) of the carrier gas must be taken into account. Pressure in the evacuation vessel varies with time but is nearly uniform. Temperature in the evacuation vessel is nearly uniform and invariant with time; *i.e.*, it seems reasonable to assume that the gas-powder mixture stays at room temperature inside the vessel. Levels of pressure and temperature in the vessel indicate that an ideal gas equation of state is appropriate for the helium carrier gas. Experimental measurements and TOPAZ calculations indicated that the injection of gas into the vessel

is choked for the range of flow rates considered. The size of the inlet relative to the vessel diameter is extremely small suggesting that gas injection could appear as a point source for flow to an observer some distance away from the inlet. If this is true it may be possible to specify a subsonic inlet boundary condition that preserves the mass flow rate. This would likely result in a calculation that is easier to converge. The computational space should include the powder evacuation vessel and the annular exit tube that carries the two phase flow mixture to the ambient. Significant pressure drop occurs in the exit tube. Computing the pressure drop is important to computing the exit flow rates. The exit boundary condition should preserve a one atmosphere total pressure for the gas stream. Care must be taken if the gas exit flow becomes sonic which was shown to be true for the end of Test 12.

This Page Intentionally Blank

2. BASELINE MODEL

The baseline gas-solid flow model chosen for implementation into is described in this chapter. The model is isothermal and compressible in the sense that the gas-phase density, $\tilde{\rho}_g$, is a function of the spatially-averaged pressure in the domain. The baseline model is essentially the model described in the CFX-5.7 theory manual [8] as the inhomogeneous multi-phase flow model.

2.1. Continuity

The continuity equations for the gas and solid phases are

$$\frac{\partial}{\partial t}\left(\varepsilon_g \tilde{\rho}_g\right)+\nabla\cdot\left(\varepsilon_g \tilde{\rho}_g \vec{v}_g\right)=0 \tag{2.1}$$

$$\frac{\partial}{\partial t}\left(\varepsilon_s \tilde{\rho}_s\right)+\nabla\cdot\left(\varepsilon_s \tilde{\rho}_s \vec{v}_s\right)=0 \tag{2.2}$$

where ε_g is the volume fraction of gas (volume of gas)/(volume of mixture); $\tilde{\rho}_g$ is the intrinsic gas density (mass of gas)/(volume of gas); $\vec{v}_g$ is the average velocity of the gas phase; ε_s is the volume fraction of solid (volume of solid)/(volume of mixture); $\tilde{\rho}_s$ is the intrinsic solid density (mass of solid)/(volume of solid); $\vec{v}_s$ is the average velocity of the solid phase. Equation (2.2) could be rewritten as

$$\frac{\partial}{\partial t}\left(\varepsilon_s\right)+\nabla\cdot\left(\varepsilon_s \vec{v}_s\right)=0 \tag{2.3}$$

since $\tilde{\rho}_s$ is a constant.

2.2. Equation of State

The intrinsic gas phase density, $\tilde{\rho}_g$, is related to the gas phase pressure, P_g, by the ideal gas equation of state

$$\tilde{\rho}_g = \frac{P_{g_{avg}}}{R_g T} \tag{2.4}$$

where $P_{g_{avg}}$ is the spatially-averaged gas phase pressure in the domain and R_g is the gas constant of the particular gas (not the universal gas constant).

2.3. Momentum

The momentum conservation equations for the gas and solid phases are

$$\frac{\partial}{\partial t}\left(\varepsilon_g \tilde{\rho}_g \vec{v}_g\right)+\nabla\cdot\left(\varepsilon_g \tilde{\rho}_g \vec{v}_g \vec{v}_g\right)=-\varepsilon_g \nabla P_g+\nabla\cdot\left(\varepsilon_g \tilde{\tilde{\tau}}_g\right)+\varepsilon_g \tilde{\rho}_g \vec{g}+\beta\left(\vec{v}_s-\vec{v}_g\right)+\vec{F}_{td} \qquad (2.5)$$

$$\frac{\partial}{\partial t}\left(\varepsilon_s \tilde{\rho}_s \vec{v}_s\right)+\nabla\cdot\left(\varepsilon_s \tilde{\rho}_s \vec{v}_s \vec{v}_s\right)=-\varepsilon_s \nabla P_g-\nabla P_s+\nabla\cdot\left(\varepsilon_s \tilde{\tilde{\tau}}_s\right)+\varepsilon_s \tilde{\rho}_s \vec{g}-\beta\left(\vec{v}_s-\vec{v}_g\right)-\vec{F}_{td} \qquad (2.6)$$

The transient and convective terms form the left hand sides of equations (2.5) and (2.6); the terms on the right hand sides are discussed below. These two equations assume that P_g includes the hydrostatic part of the pressure field. It is more traditional to express the momentum equation for the gas phase in a form that explicitly splits P_g into hydrostatic and motion pressure components, for example:

$$\frac{\partial}{\partial t}\left(\varepsilon_g \tilde{\rho}_g \vec{v}_g\right)+\nabla\cdot\left(\varepsilon_g \tilde{\rho}_g \vec{v}_g \vec{v}_g\right)=-\varepsilon_g \nabla P_g+\nabla\cdot\left(\varepsilon_g \tilde{\tilde{\tau}}_g\right)+\varepsilon_g (\tilde{\rho}_g-\tilde{\rho}_{g_{ref}})\vec{g}+\beta\left(\vec{v}_s-\vec{v}_g\right)+\vec{F}_{td} \qquad (2.7)$$

$$\frac{\partial}{\partial t}\left(\varepsilon_s \tilde{\rho}_s \vec{v}_s\right)+\nabla\cdot\left(\varepsilon_s \tilde{\rho}_s \vec{v}_s \vec{v}_s\right)=-\varepsilon_s \nabla P_g-\nabla P_s+\nabla\cdot\left(\varepsilon_s \tilde{\tilde{\tau}}_s\right)+\varepsilon_s (\tilde{\rho}_s-\tilde{\rho}_{g_{ref}})\vec{g}-\beta\left(\vec{v}_s-\vec{v}_g\right)-\vec{F}_{td} \qquad (2.8)$$

Equations (2.7) and (2.8) show this splitting while keeping the same symbol for gas-phase pressure P_g. For most gas-solid systems equations (2.5) and (2.6) are nearly equivalent to (2.7) and (2.8). However for denser continuous phases (e.g., water) it is important to use the latter equations.

The gas phase pressure gradient is applied to both gas and solid phase momentum equations as indicated by the first terms on the right hand sides of these equations. The gas and solid phase stress tensors are given by

$$\tilde{\tilde{\tau}}_g=\mu_{g_{eff}}\left(\nabla\vec{v}_g+\nabla\vec{v}_g{}^T\right) \qquad (2.9)$$

and

$$\tilde{\tilde{\tau}}_s=\mu_{s_{eff}}\left(\nabla\vec{v}_s+\nabla\vec{v}_s{}^T\right) \qquad (2.10)$$

where initially we follow the approach suggested in CFX-5.7, *i.e.*,

$$\mu_{s_{eff}}=C_{t_s}\mu_{g_{eff}} \qquad (2.11)$$

In equation (2.11) C_{t_s} is a constant to be specified by the user (default value is zero). The determination of $\mu_{g_{eff}}$ will be discussed in the turbulence model section.

The terms $\varepsilon_g \tilde{\rho}_g \vec{g}$ and $\varepsilon_s \tilde{\rho}_s \vec{g}$ in equations (2.5) and (2.6) are the body force terms.

The term $\beta\left(\vec{v}_s-\vec{v}_g\right)$ in equations (2.5) and (2.6) represents the inter-phase momentum transfer due to drag. For dilute flow ($\varepsilon_s \leq 0.2$) the inter-phase friction coefficient β is given by Wen and Yu [12].

$$\beta=\frac{3}{4}C_d\frac{\varepsilon_g\varepsilon_s\tilde{\rho}_g\left|\vec{v}_g-\vec{v}_s\right|}{d_s}\varepsilon_g^{-2.65} \tag{2.12}$$

where

$$C_d=\frac{24}{\mathrm{Re}_s}\left(1+0.15\,\mathrm{Re}_s^{0.687}\right) \quad \text{for } \mathrm{Re}_s<1000 \tag{2.13}$$

and

$$C_d=0.44 \quad \text{for } \mathrm{Re}_s>1000 \tag{2.14}$$

and where

$$\mathrm{Re}_s=\frac{\varepsilon_g\tilde{\rho}_g d_s\left|\vec{v}_s-\vec{v}_g\right|}{\tilde{\mu}_g} \quad . \tag{2.15}$$

For dense flow ($\varepsilon_s>0.2$) the inter-phase friction coefficient β is given by Ergun [9]

$$\beta=150\frac{\varepsilon_s^{\,2}\tilde{\mu}_g}{\varepsilon_g d_s^{\,2}}+1.75\frac{\tilde{\rho}_g\varepsilon_s\left|\vec{v}_g-\vec{v}_s\right|}{d_s} \quad . \tag{2.16}$$

NOTE: although the inter-friction coefficient β given here appears to have an additional multiplying factor of ε_g compared with some models in the literature (Gidaspow [10], p. 217, Table 8.1; p. 40, equation 2.27; Neri and Gidaspow, [11]), an examination of the correlation and experiment of Wen and Yu [12] show that their drag expression was obtained from a momentum balance on particulate fluidization in a tube flow where the pressure drop did not include an ε_g factor. Since this factor is included in the momentum balance given here in equation (2.5), the inclusion of what appears to be an additional ε_g multiplying factor in the expression for β is consistent.

The term F_{td} in equations (2.5) and (2.6) represents the turbulent dispersion force per unit volume of the mixture and is given by Burns *et. al.* [7] as

$$F_{td}=\beta\frac{\nu_t}{\sigma_t}\left(\frac{\nabla\varepsilon_s}{\varepsilon_s}-\frac{\nabla\varepsilon_g}{\varepsilon_g}\right) \quad . \tag{2.17}$$

The constant σ_t is defined in the CFX-5.7 theory manual [8] as the turbulent Schmidt number for volume fraction. This constant is to be accessible to users in order to allow

testing of the influence of turbulent dispersion on momentum transport. The default value of this constant is suggested to be 0.9 in the CFX-5.7 manual.

There are a number of methods of modeling the effect of solid pressure on solid phase momentum transport (the term ∇P_s in equation (2.6)). These methods range from empirical expressions to complex expressions based on a granular temperature concept from kinetic theory. Our baseline model makes use of a relatively simple empirical expression suggested by Gidaspow [10]. This model defines the solid phase pressure by

$$\nabla P_s = G(\varepsilon_s)\nabla \varepsilon_s \qquad \text{where} \quad G(\varepsilon_s) = \frac{\partial P_s}{\partial \varepsilon_s} \tag{2.18}$$

and where

$$G(\varepsilon_s) = G_o e^{\left[c\left(\varepsilon_s - \varepsilon_{s_{\max}}\right)\right]} \quad . \tag{2.19}$$

G_o is the reference elasticity modulus, $c = 20$ to 600 is the compaction modulus, and $\varepsilon_{s_{\max}}$ is the maximum packing parameter [8]. For the solid phase, typical values for $\varepsilon_{s_{\max}}$ should range from 0.5 to 0.74, the latter being the maximum possible packing for solid spheres. With this model it is possible for the maximum solid phase volume fraction to be larger than $\varepsilon_{s_{\max}}$. Hence CFX recommends using 0.62 as a default value for $\varepsilon_{s_{\max}}$ when modeling solid spheres. The reference elasticity modulus G_o and the maximum packing parameter $\varepsilon_{s_{\max}}$ should be user accessible. Default values should be 1 Pa and 0.62, respectively. The compaction modulus c should also be accessible to the user and have a default value of 100.

2.4. Energy

We recognize that for our application the incoming gas flow is compressible. We estimate incoming Mach numbers will vary between 0.4 and 0.5. Hence when the gas speed decreases the temperature of the gas will increase. However, the influence of this temperature increase on the two-phase flow quantities of interest may be of second order importance. For this reason we have chosen to assume isothermal gas-solid flow for the baseline model. It may be necessary to add the energy equations for the solid and gas phases at a later time.

2.5. Turbulence

The two-equation turbulence model for multi-phase flow in CFX-5.7 is based on the standard $k-e$ model applied to the gas phase. The model can be summarized as follows:

$$\mu_{g_{eff}} = \varepsilon_g \tilde{\mu}_g + \mu_{t_g} \tag{2.20}$$

$$\mu_{t_g} = C_\mu \tilde{\rho}_g \frac{k_g^{\,2}}{e_g} \tag{2.21}$$

$$\frac{\partial}{\partial t}\left(\varepsilon_g \tilde{\rho}_g k_g\right)+\nabla\cdot\left(\varepsilon_g \tilde{\rho}_g \vec{v}_g k_g\right)=\nabla\cdot\left[\varepsilon_g\left(\tilde{\mu}_g+\frac{\mu_{t_g}}{\sigma_k}\right)\nabla k_g\right]+\varepsilon_g\left(P_g-\tilde{\rho}_g e_g\right)+T_{(g-s)_k} \quad (2.22)$$

$$\frac{\partial}{\partial t}\left(\varepsilon_g \tilde{\rho}_g e_g\right)+\nabla\cdot\left(\varepsilon_g \tilde{\rho}_g \vec{v}_g e_g\right)=\nabla\cdot\left[\varepsilon_g\left(\tilde{\mu}_g+\frac{\mu_{t_g}}{\sigma_e}\right)\nabla e_g\right]+\varepsilon_g\frac{k_g}{e_g}\left(C_{e_1}P_g-C_{e_2}\tilde{\rho}_g e_g\right)+T_{(g-s)_e} \quad (2.23)$$

where k is the turbulent kinetic energy and e is the dissipation rate of turbulent kinetic energy (commonly assigned the symbol ε but not here due to the use of ε for volume fraction). The inter-phase transfer terms, $T_{(g-s)_k}$ and $T_{(g-s)_e}$, are omitted in the CFX treatment. This approach is taken in the baseline model described here.

2.6. Parameters

In summary, the following parameters are required in the baseline gas-solid model: intrinsic solid-phase density $\tilde{\rho}_s$; solid particle diameter d_s; reference elastic modulus G_o; compaction modulus c; maximum packing parameter $\varepsilon_{s_{\max}}$; turbulent Schmidt number for volume fraction σ_t; $k-e$ turbulence model parameters C_μ, σ_k, σ_e, C_{e_1}, C_{e_2}; effective solid phase viscosity multiplier C_{t_s}.

2.7. Initial Conditions

The following initial conditions are required in the baseline gas-solid model:

1. Set initial value of solid-phase volume fraction (NOTE: for locations where the solid phase is not present a nonzero value of the solid phase volume fraction should be set, *e.g.*, something much larger than machine zero but much smaller than expected values, recommended in CFX manual).
2. Set initial value of gas pressure.
3. Set initial values of gas phase velocity.
4. Set initial values of solid phase velocity.
5. Set the temperature.
6. Set the initial values of gas phase turbulence variables k_g and e_g.

2.8. Boundary Conditions

The following boundary conditions are required in the baseline gas-solid model:

1. free-slip at walls for the solid phase.
2. no-slip at walls for the gas phase.
3. volume fraction of solid phase (ε_s) at inlet and open boundaries; volume fraction of gas phase is given by $\varepsilon_g = 1-\varepsilon_s$.

4. inlet mass flow rates: $\dot{m}_{g_{in}} = \tilde{\rho}_g \int_{A_{in}} \varepsilon_g \vec{v}_g \cdot \hat{n} dA$ and $\dot{m}_{s_{in}} = \tilde{\rho}_s \int_{A_{in}} \varepsilon_s \vec{v}_s \cdot \hat{n} dA$. For assumed uniform profiles at the inlet, given the mass flow rates of the gas and solid phases, these expressions can be used to determine the inlet velocities of the phases.
5. gas pressure or Mach number constraint at outflow boundary.

3. TEST PROBLEMS

Our model development plan seeks to improve FUEGO capabilities by addressing a series of problems each having an increased level of physical complexity. The series of modeling problems and the issues they address are shown in Figure 21. The gas vessel blowdown problem and the De Laval nozzle flow problem will be used to access the accuracy and robustness of the newly implemented compressible flow features in FUEGO. The first multi-phase problem to be solved (Darcy porous media flow) will be one in which the solid phase remains stationary, thus eliminating the need to account for solid phase momentum. Fluidized bed and multiphase tube flows will then be addressed. These problems exhibit all the complexities of the powder evacuation problem but the geometry is greatly simplified. Finally we will address the powder evacuation problem in a geometry of interest.

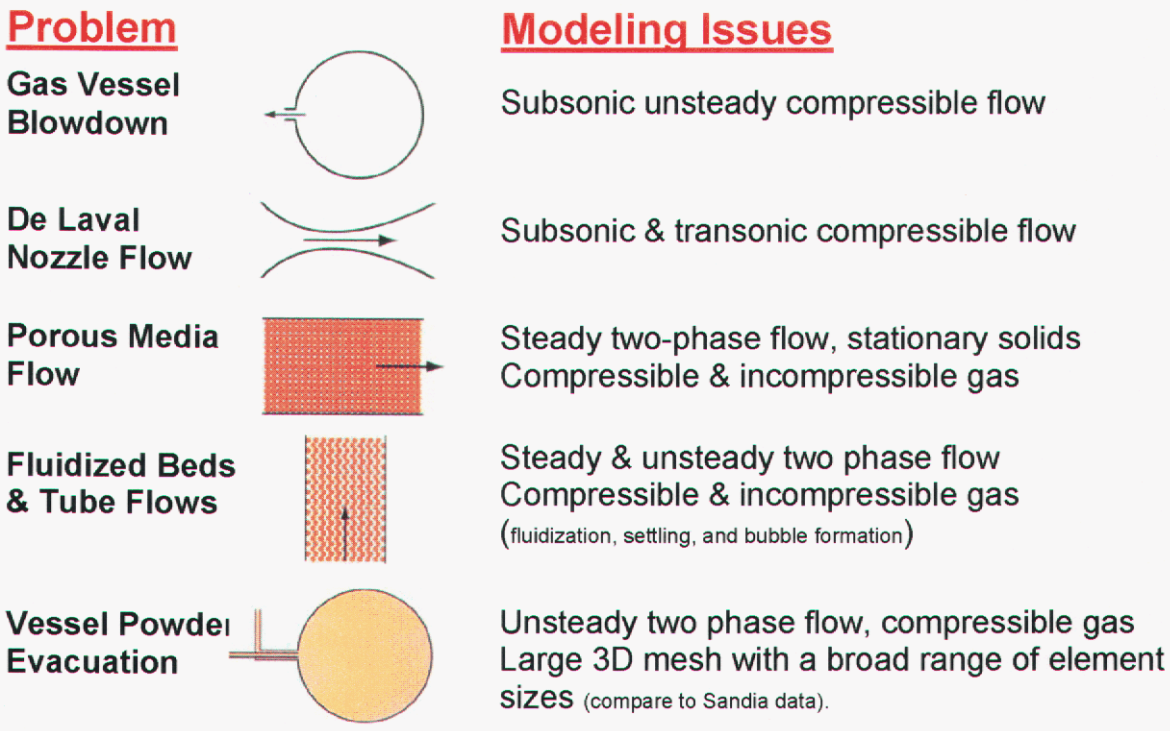

Figure 21. Multi-phase model development plan.

The remaining subsections in this chapter document computational results and problems encountered in developing the multiphase capability for FUEGO. In the last subsection we summarize the development and a computational mesh suitable for performing powder evacuation calculations.

3.1. Vessel Blowdown

Vessel blowdown calculations were made to test the newly added compressible flow capability in FUEGO. The blowdown problem is useful since an analytical solution is available from Bird, Stewart and Lightfoot [13] and others. The vessel blowdown problem is schematically represented in Figure 22 and is subject to the following assumptions:

- Gas properties in vessel are uniform
- Adiabatic vessel walls
- Isentropic 1-D acceleration from 1 to 2 (ideal nozzle)
- Gas is thermally and calorically perfect
- External ambient conditions constant

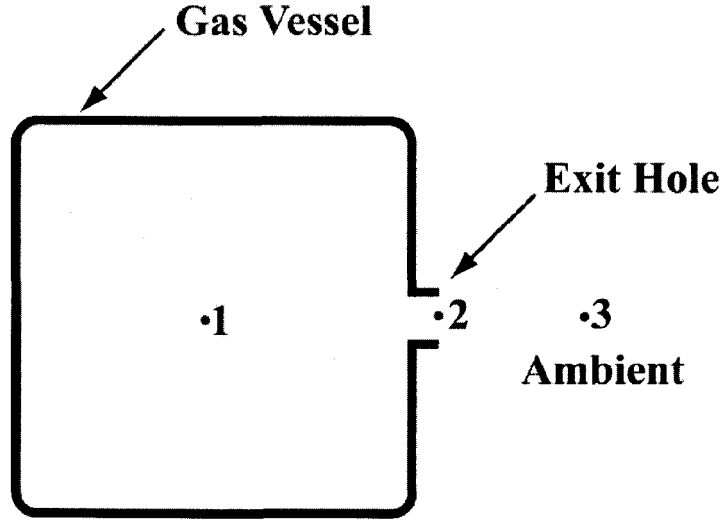

Figure 22. Schematic of the vessel blowdown problem.

Our blowdown calculations were restricted to subsonic flow at the outlet. Under these conditions,

$$P_2 = P_3 \tag{3.1}$$

Bird, Stewart and Lightfoot show that the following expression can be used to describe the vessel blowdown

$$V\frac{d\rho_1}{dt} = -A_2\sqrt{2P_1\rho_1\left[\left(\frac{\gamma}{\gamma-1}\right)\left(\frac{P_2}{P_1}\right)^{\frac{2}{\lambda}} - \left(\frac{P_2}{P_1}\right)^{\frac{\gamma+1}{\gamma}}\right]} \tag{3.2}$$

where

$$P_1\rho_1^{-\gamma} = P_1(0)\rho_1(0)^{-\gamma} \quad . \tag{3.3}$$

Bird, Stewart, and Lightfoot integrate Equation (3.2) to obtain two integral equations that can be used to predict vessel pressure as a function of time. The two expressions represent the sonic and subsonic branches of the solution. For the subsonic case in which Equation (3.1) is valid, Equation (3.2) may be numerically integrated in time using a variety of explicit methods to yield the pressure history as a function of time. We used this method when comparing FUEGO solutions to the Bird, Stewart and Lightfoot solution.

A number of subsonic two-dimensional vessel blowdown calculations were conducted using FUEGO with the mesh shown in Figure 23. Quad meshes ranging from 12,500 to 50,000 elements were used. Time steps were varied from 10^{-5} to 5×10^{-5} seconds. The initial pressure ratio (vessel/ambient) was assumed to be 1.01 and the vessel volume to area ratio was 10^{6} cm. A sharp edge opening was used as indicated by the red line in Figure 23.

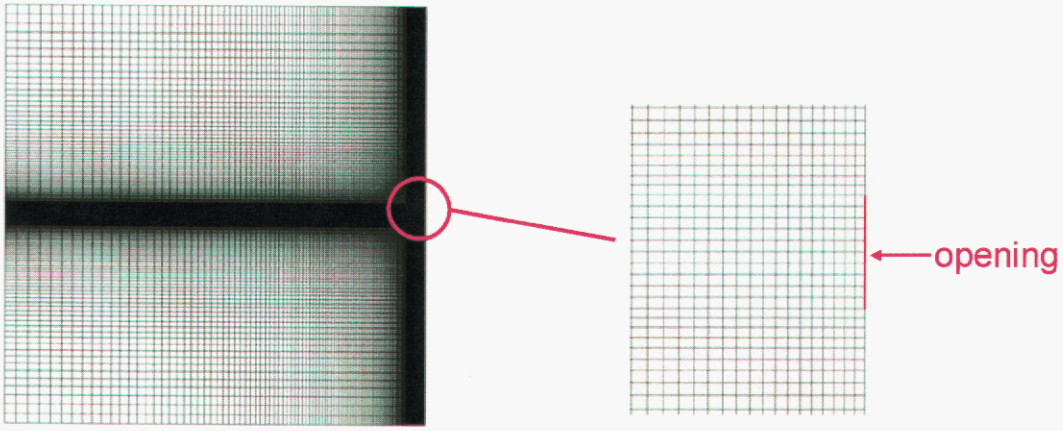

Figure 23. Computational mesh for vessel blowdown studies.

FUEGO generated pressure decays tended to be longer than those predicted by the Bird, Stewart and Lightfoot (BSL) solution. The top two decompression transients (solid orange and solid green lines) shown in Figure 24 are typical of the results predicted by FUEGO. The pressure transients tended to be above the transient predicted by the BSL solution (lowest red line) for the entire time of the vessel blowdown regardless of the mesh density and time steps used in the FUEGO calculations.

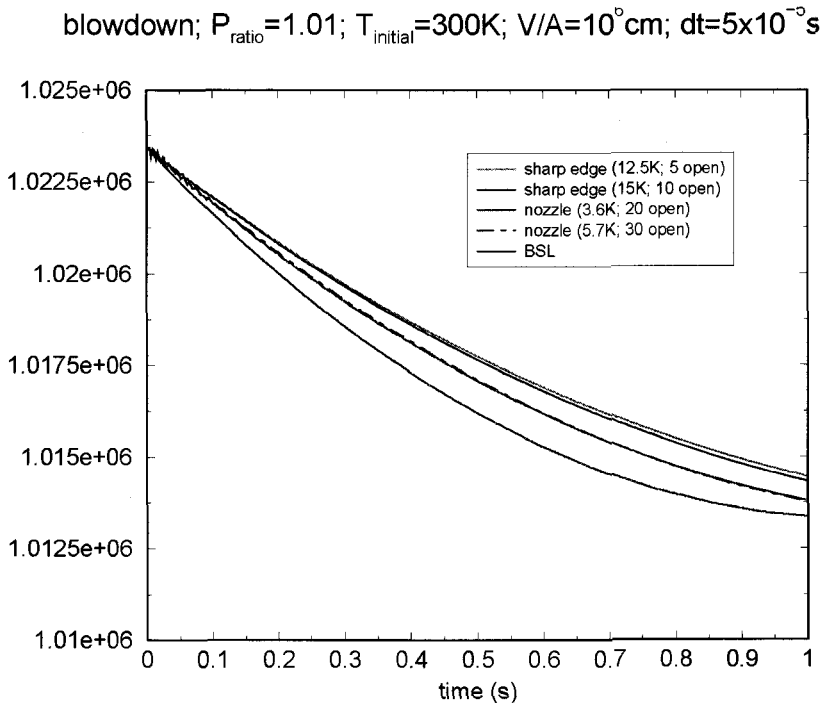

Figure 24. Predicted vessel decompression transients.

It was suspected that the FUEGO simulations were violating one of the principle assumptions of the BSL solution, the isentropic one-dimensional acceleration of the gas from the interior of the vessel to the exit. Because FUEGO accounts for two-dimensional effects and includes the influence of viscosity, it was felt that the computed flow through the sharp edged exit hole was unlikely to resemble the "plug flow" required by the BSL solution. To test this theory the exit hole was redesigned to provide a more gradual transition to the exit as shown in the right half of Figure 25.

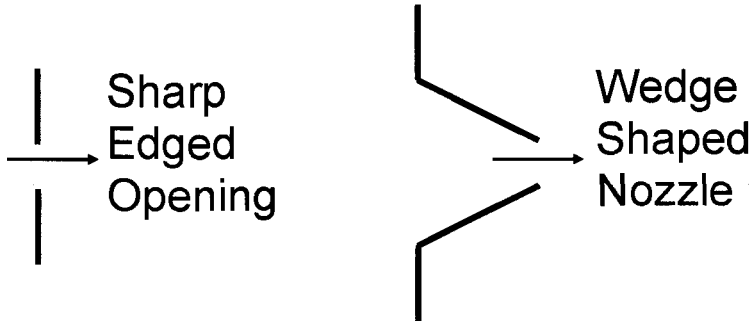

Figure 25. Two vessel discharge geometries.

Calculations made with the new exit design, while not perfect, tended to produce a more plug-like flow at the exit. Figure 26 shows the exit hole velocity distributions for the sharp edged orifice and the nozzle. The velocity profile for the nozzle is nearly flat or

"plug-like" over ninety percent of the opening. The velocity distribution for the sharp edged orifice is parabolic.

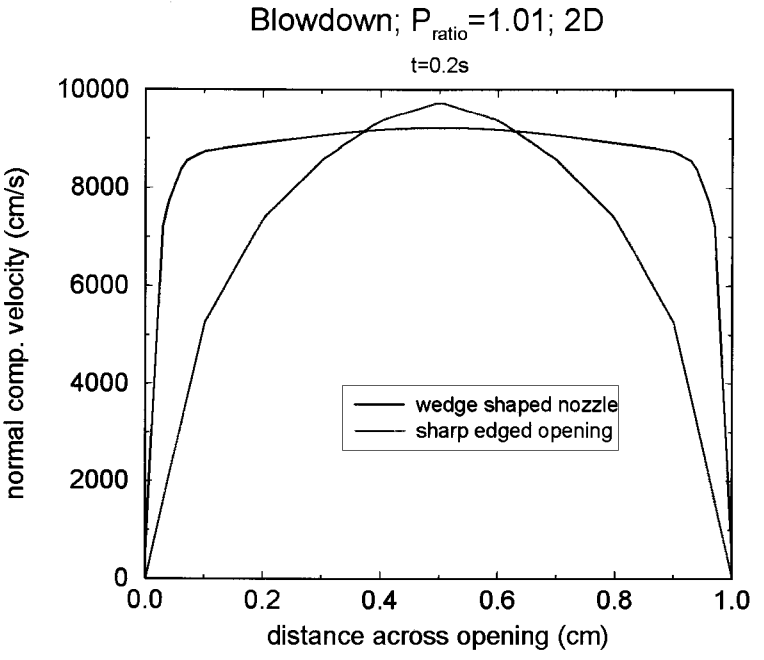

Figure 26. Velocity distributions across the vessel exit hole for two opening designs.

FUEGO-computed blowdown calculations using the new opening design produced pressure transients that were significantly closer to the BSL solution. Two such calculations for two different mesh densities are shown in Figure 24 (the green dashed line and the blue line). It is believed that further refinement of the exit nozzle, lowered viscosity and slip walls will produce results that are even closer to the BSL solution.

3.2. De Laval Nozzle Flow

Developer, Greg Wagner, 08757, formulated a De Laval nozzle problem to assess the accuracy and robustness of the compressible flow capability in FUEGO. The problem is useful as a verification tool since an analytical solution exists for inviscid, one-dimensional, steady, compressible flow through a De Laval nozzle.

The Mach number distribution from the FUEGO solution of the De Laval nozzle flow at steady flow conditions is shown in Figure 27. The computational region is a planar nozzle one element thick with symmetry applied to the planes parallel to the paper. A hex mesh is used to capture the flow field. The inflow boundary condition is on the left end. Here temperature and velocity are set to provide an inlet Mach number of 0.16. The static pressure at the exit on the right is fixed. Free slip is permitted on the nozzle walls and an air ideal gas equation of stated is used to represent the flowing gas. The results show that the peak Mach number occurs at the throat or the narrowest point in the nozzle. This is to

be expected since the flow is subsonic. The maximum Mach number is approximately 0.34. The black vertical lines superimposed over the nozzle are lines of constant Mach number. Note that these lines become curved as they approach the center of the nozzle. In a true one-dimensional flow, these lines would be straight and vertical throughout the flow. The lines are curved here because FUEGO is solving the full three-dimensional problem. The flow turns relative to the nozzle centerline as it enters and exits the throat region. This multi-dimensional behavior causes the lines of constant Mach number to take on the curved appearance shown in Figure 27.

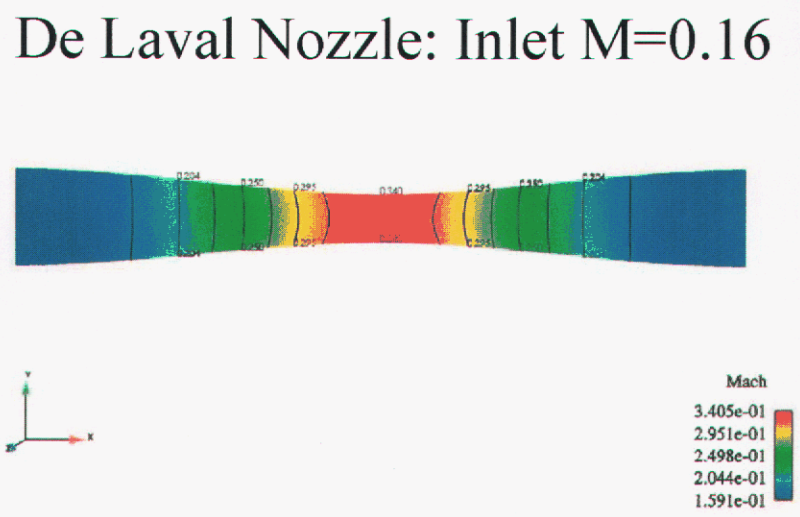

Figure 27. Mach number distribution in Laval nozzle.

The centerline pressure and Mach number distributions computed by FUEGO are compared to the one-dimensional analytical solution in Figure 28 and Figure 29 respectively. The agreement is excellent. Small variations between the two curves are likely due to the fact that FUEGO accounts for multidimensional features in the flow. Furthermore, although slip was imposed at the walls, the FUEGO calculations included the effects of fluid viscosity which are not accounted for in the analytical solution.

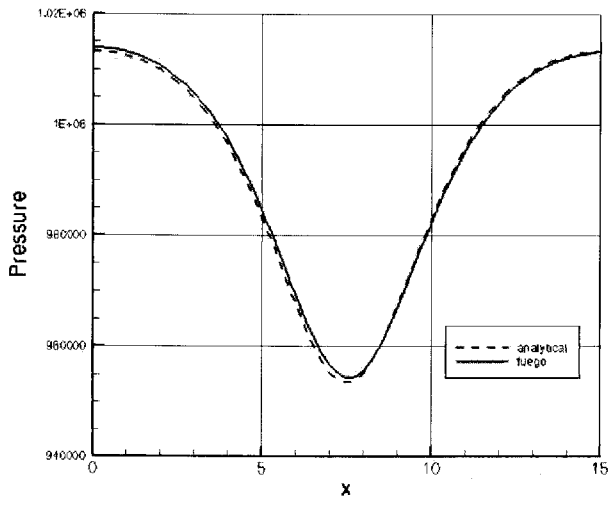

Figure 28. Pressure distribution along the centerline of the Laval nozzle.

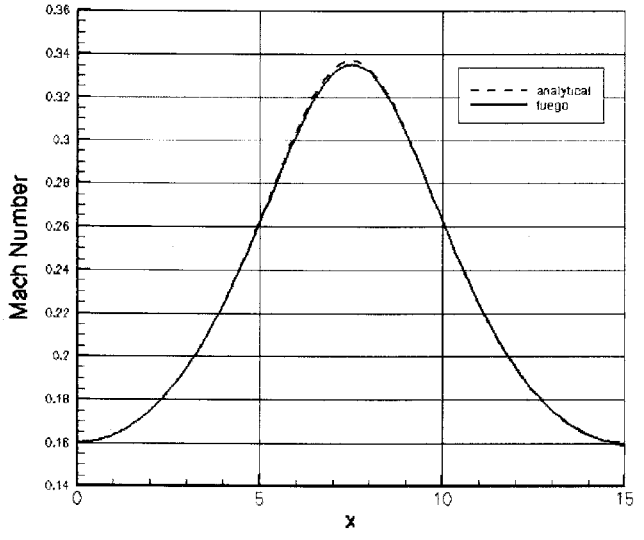

Figure 29. Mach number distribution along the centerline of the Laval nozzle.

Robust solutions and accurate results were obtained for compressible nozzle flows having maximum Mach numbers as high as 0.35. However, for higher speed flows, calculations tended to become unstable and no solutions could be obtained. A one-dimensional prototyping code was developed to explore stability issues. At this writing it is believed that the flow instabilities result from the way entrance and exit flow boundary conditions are implemented.

3.3. Darcy Flow Through a Stationary Porous Medium

The first multiphase flow problem solved using FUEGO's new multiphase flow model was flow through a porous medium. This problem is unique in that it permits an examination of the multiphase flow implementation without having to solve the solid phase momentum equation. Furthermore there is a simple analytical solution for low speed porous media flows that can be used to verify some aspects of the multiphase flow implementation. Porous media flow problems discussed here are restricted to incompressible laminar gas or fluid flowing through a homogeneous stationary solid matrix (uniform solid volume fraction) as depicted in Figure 30.

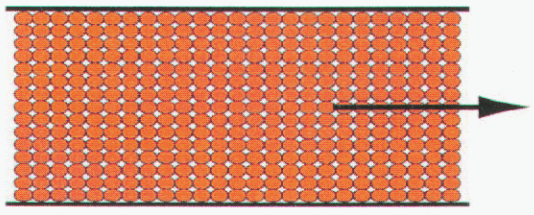

Figure 30. Flow of an incompressible gas through a uniform stationary porous media.

3.3.1 Description of the Problem

Darcy's law describes steady, creeping flow through a stationary porous medium:

$$q = -\frac{k}{\tilde{\mu}_g}\frac{dP}{dx} \tag{3.4}$$

where q is the specific discharge rate (volume flow rate per unit of total cross-sectional area; note $q = \varepsilon_g u_g$ where u_g is the fluid velocity component in the x direction) and k is the permeability of the medium. This expression can be derived from the fluid momentum equation (2.5) by neglecting the transient, inertial, stress, body force, and turbulent dispersion force terms. The x component of momentum then becomes

$$\varepsilon_g \frac{dP_g}{dx} = \beta\left(u_s - u_g\right) \tag{3.5}$$

For a porous medium where there is a significant solid volume fraction β is given by equation (2.16). For creeping flow through a stationary porous medium with significant solid volume fraction, the second term in equation (2.16) is negligible compared with the first term. Substituting the reduced expression for β into equation (3.5) and rearranging gives

$$\varepsilon_g u_g = -\frac{\varepsilon_g^3 d_s^2}{150\varepsilon_s^2 \tilde{\mu}_g}\frac{dP_g}{dx} \tag{3.6}$$

Comparing with equation (3.4) we see that an expression for k is

$$k = \frac{\varepsilon_g^3 d_s^2}{150\varepsilon_s^2} \tag{3.7}$$

It is noted that the Kozeny-Carman equation given in Bear [14] for the permeability of a porous medium of constant diameter spheres is

$$k_{\text{K-C}} = \frac{\varepsilon_g^3 d_s^2}{180\varepsilon_s^2} \tag{3.8}$$

The test problem proposed for solution is one-dimensional, steady, creeping flow through a stationary bed of spheres packed in a cubic arrangement (the least compact arrangement). Let the spheres have diameter $d_s = 100\ \mu m$ (0.01 cm); the porosity is $\varepsilon_g = 0.4764$. Equation (3.7) then gives a permeability $k = 2.63\text{x}10^{-7}$ cm^2. Assume a channel geometry with channel height of 100 particle diameters or 1 cm and channel length of 10 cm. Let the channel surfaces be slip surfaces to simulate the one-dimensional flow behavior. Assuming a Reynolds number of unity the specific discharge rate is

$$q = \frac{\text{Re}\cdot\nu}{d_s} = 15.94 \text{ cm/s} \tag{3.9}$$

for air at atmospheric pressure and 300 K. Solving equation (3.4) for the pressure drop gives $1.1322\text{x}10^5$ dynes/cm^2 over a 10 cm length of porous medium. Apply this pressure drop to the channel and solve the flow problem. The resulting air velocity should be close to 33.5 cm/s.

FUEGO result

A FUEGO calculation was made for the above conditions with a pressure drop equal to the above determined value. The resulting velocity calculated in FUEGO was 32.75 cm/s, which is within 2% of the analytical value of 33.5 cm/s, given above. One reason for the difference is that the drag expression in FUEGO includes the second term in equation (2.16) which depends on the particle Reynolds number. A second case was computed in which the particle Reynolds number was reduced by one order of magnitude, from 1 to 0.1. This resulted in a velocity computed in FUEGO of 3.34 cm/s, which is within 0.3% of the analytical value of 3.35 cm/s.

3.4. Powder Evacuation from Channel

FUEGO developer, Stefan Domino, 01541, formulated a channel flow problem to demonstrate the fully functional baseline two-phase flow model (without turbulence). In this problem 20 cm long channel with a square cross-section (2 cm x 2 cm) is filled with stationary and uniformly distributed (volume fraction .15) 100 micron spherical particles. At time zero an incompressible gas is introduced into one end of the channel with a constant velocity of 0.1 cm/s. No-slip boundaries were provided for the interior walls of the channel. The computational mesh for this problem is shown in Figure 31. Uniform hex elements are used in the mesh.

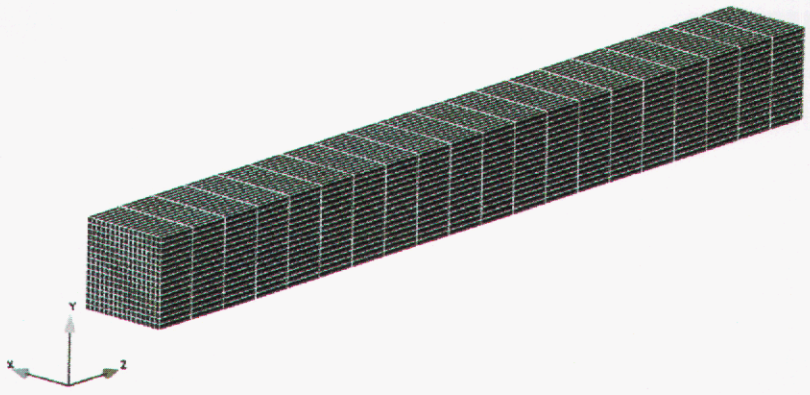

Figure 31. Computational mesh for the powder evacuation problem.

Results from the transient simulation up to a time of 100 seconds are shown in Figure 32.

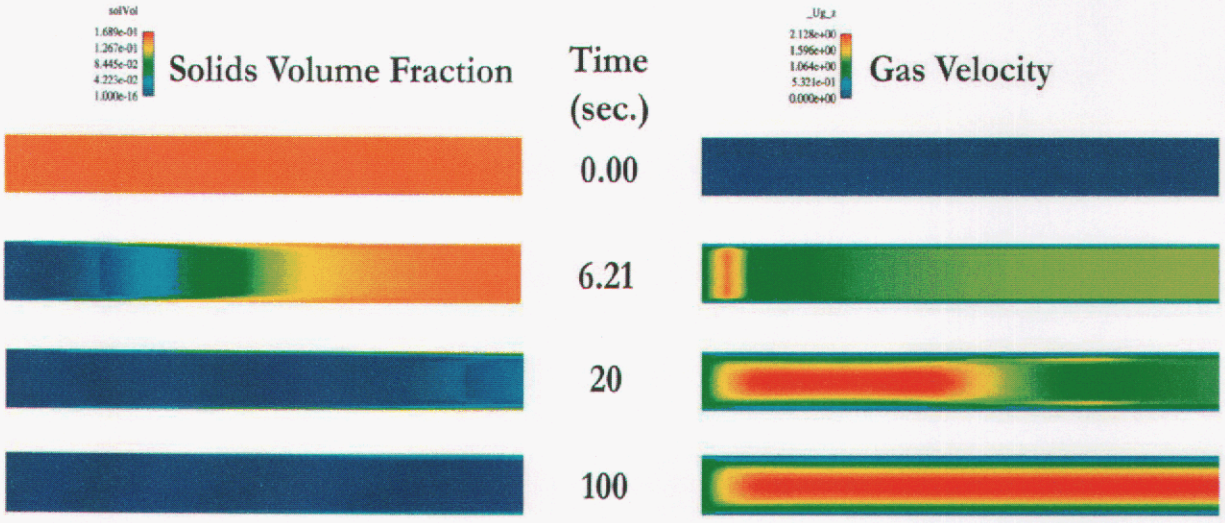

Figure 32. Channel cross-sections at four times.

The right side of Figure 32 shows cross-sections of solid volume fraction at 0., 6.21, 20. and 100. seconds. Corresponding cross-sections of axial gas velocity are shown on the right side of the figure. Since zero slip is enforced at the channel walls, the resulting gas phase velocity distribution is parabolic. This is most evident in the axial gas velocity distribution shown at 100 seconds when all the solids have been evacuated and flow approaches steady-state. Even during the evacuation transient cross-sectional gas velocity gradients give rise to corresponding gradients in the solid phase velocity and hence the solid phase volume fraction. The calculations show that the last solids to leave any cross-section along the channel are the solids adjacent to the walls. Had a free slip boundary condition been imposed at the walls one would have expected the powder evacuation to resemble a plug flow. The evacuation of powder is clearly visible as the gas flows from left to right in the channel.

The channel powder evacuation problem provides qualitative verification that the baseline multiphase flow model is functioning properly.

3.5. Vertical Fluidized Bed Flow in Tube

FUEGO's baseline multiphase flow model was used to simulate the fluidized bed experiments of Moritomi et al. [15]. The geometry for the fluidized bed is depicted in Figure 33. The figure (not to scale) shows a vertically oriented circular tube 20 cm long and 5 cm in diameter. Initially the tube is filled with glass beads uniformly distributed with a volume fraction of .104. At time zero the beads are allowed to fall downward under the influence of gravity while a steady flow of water enters the tube from the bottom. The water enters at 0.65 cm/sec which is sufficient to fluidize the bed without causing any of the beads to exit the top end of the tube. The total mass of beads (100 g) in the tube should remain constant over time. The beads have a diameter of 163 microns and a density of 2.45 g/cm^3.

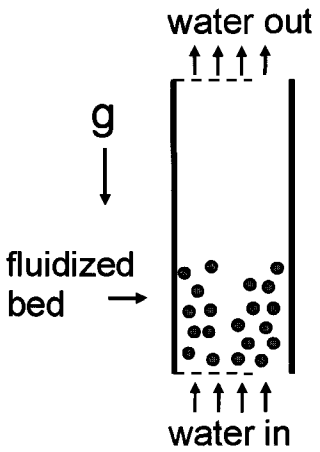

Figure 33. Fluidized bed.

The computational mesh used in the FUEGO simulation is shown in Figure 34. The mesh is composed entirely of hex elements.

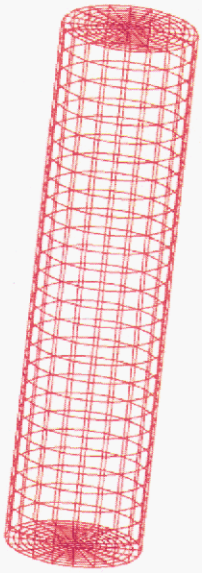

Figure 34. Computational mesh for the fluidized bed problem.

Results from the FUEGO fluidized bed simulation are shown in Figure 35 and Figure 36. For the first 30 seconds of the simulation the solids migrate downward and eventually collect in the bottom third of the cylinder. From that time on the solid volume fraction distribution is similar to that shown in Figure 35. The interface between the solid-gas mixture and the pure gas is in constant motion and small variations in solid volume fraction are evident throughout the bed. A plot of solid volume fraction along the bed centerline at 50 seconds is shown in the upper part of Figure 36. The plot shows that the bed height is approximately 7 cm. Because of the unsteady behavior of fluidized beads, the bed height fluctuates between 6.7 and 7.3 cm depending on time and location. Moritomi et al. [15] report an average bed height of 7.2 cm in their experiments which is in good agreement with the FUEGO simulation.

Close examination of the FUEGO solution shows that the mass of solids in the cylinder is not conserved. A plot showing the time history of the solids mass is shown in the lower part of Figure 36. The solid mass falls from its initial value of 100 g to 63 g over the first 35 seconds of simulation time. It then increases to 72 g at 50 seconds. The developers have been made aware of this problem and have plans to implement a new conservative method for computing the solid phase volume fraction.

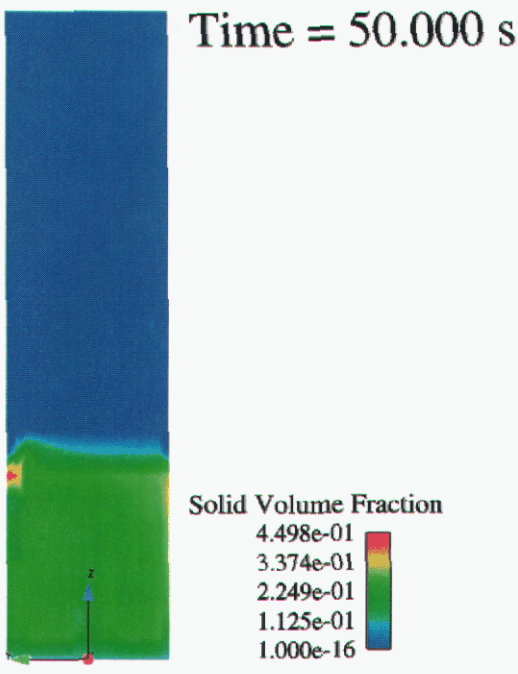

Figure 35. Fluidized bed solution at 50 seconds.

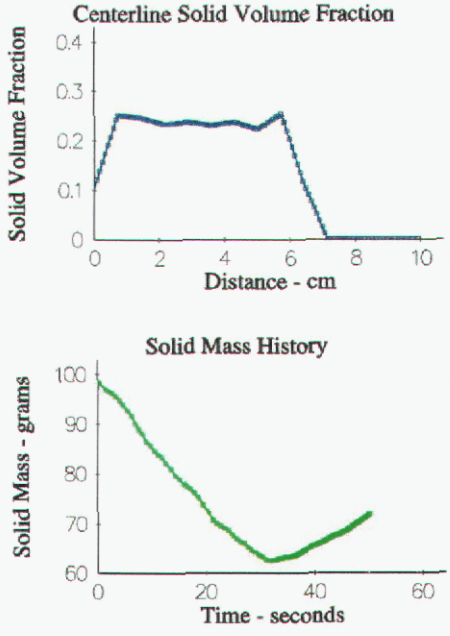

Figure 36. Centerline solid volume fraction distribution at 50 seconds and solid mass history.

3.6. Progress in Simulating Sandia Powder Evacuation Experiments

Although some development work is needed in the implementation of FUEGO multiphase flow (high Mach number compressible flow and mass conservation of the solids phase), work was begun on modeling the Sandia powder evacuation experiments conducted by Peter Van Blarigan, 08224 and Dave Zanini, 08125 in 2002 (See Chapter 1). This work consisted of developing two computational meshes and conducting a simple single phase flow simulation to insure that the meshes were properly constructed.

The first computational mesh developed for the power evacuation problem is shown here in Figure 37. It consists of 24284 hex elements and 29241 nodes. The mesh represents one quarter of the experimental powder storage vessel and one quarter of the small annular exit tube. Because the entrance and exit points are located at the centerline of the spherical powder storage vessel and the vessel was oriented such that the gravity vector aligned with this same centerline, it was possible to take advantage of symmetry and eliminate three quarters of the mesh. As a result the flat (red) surfaces shown in Figure 37 represent planes of symmetry. The inflow boundary condition is located at a flat quarter circle surface at the end of the inlet tube that extends 0.127 m into the vessel (see Chapter 1). The outflow boundary condition is located at a flat quarter annular surface at the end of the annular exit tube.

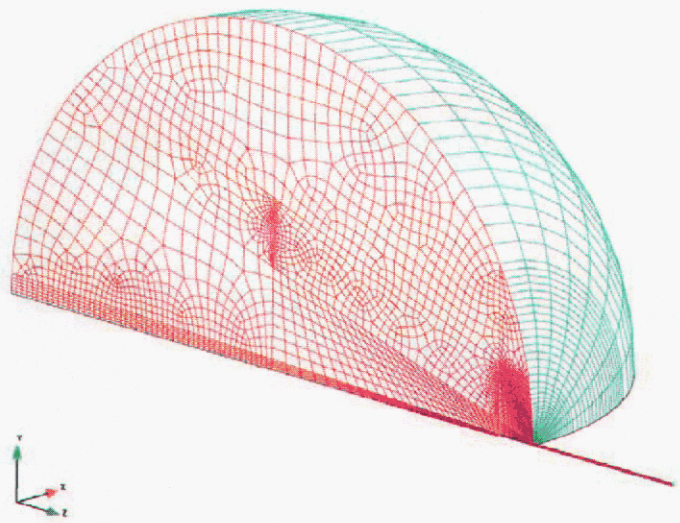

Figure 37. Computational mesh for the powder evacuation problem.

It was anticipated that the exit flow boundary condition applied at the end of the annular exit tube could prove problematic. It is known (see Chapter 1) that during the evacuation transient the flow at the end of the annular tube transitions between choked flow condition (where the flow of gas is limited by the sound speed) and a subsonic condition which requires an applied pressure at the exit boundary. Some thought was given to developing a "smart" exit flow boundary condition that could transition between sonic

and subsonic boundary conditions as required. In order to avoid this complexity a second mesh was developed that included a portion of the ambient immediately downstream of the annular tube. That mesh is shown in Figure 38 and includes 33696 hex elements and 69687 nodes. The ambient is represented by the quarter cylinder attached to the end of the annular exit tube. Red surfaces represent planes of symmetry and blue surfaces represent walls. The green surface represents the new outflow boundary which is a considerable distance from the end of the annular exit tube. Furthermore the new outflow boundary is several orders of magnitude larger in surface area than the outflow boundary of the previous mesh. As a result the flow there will be low in Mach number allowing the application of a specified pressure or the "opening" boundary condition in FUEGO. Moving the outlet boundary condition to a subsonic location means the all sonic and transonic flow will occur within the computational mesh (the region immediately downstream of the annular exit). Barring numerical difficulties, this should not be a problem for FUEGO since the transport equations are capable of capturing sonic and transonic flow.

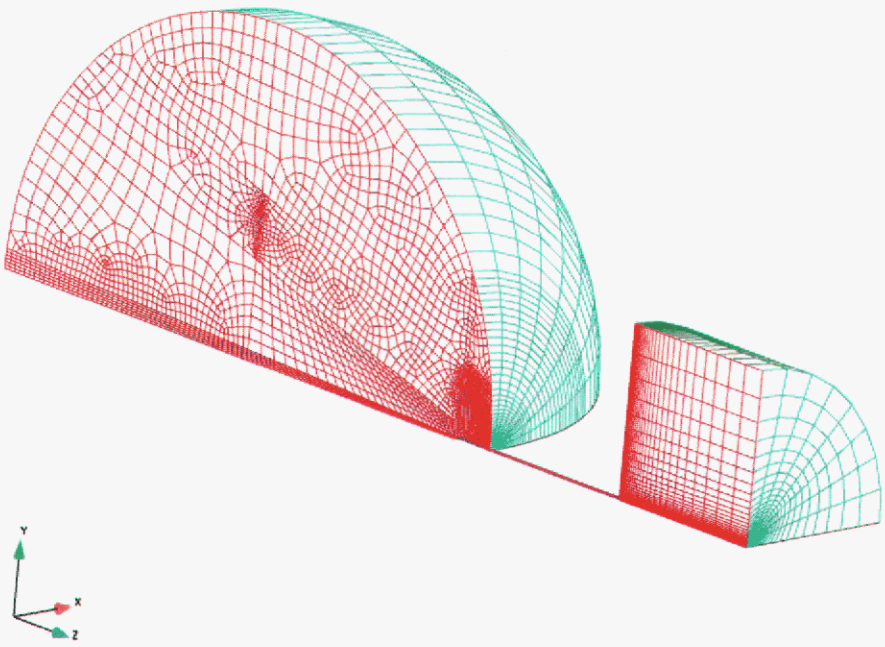

Figure 38. Computational mesh for the powder evacuation problem – ambient included.

The meshes shown in Figure 37 and Figure 38 contain a number of meshed volumes which are merged together. In order to insure that the merging was done correctly such that the interior of the vessel, exit tube, and ambient was continuous, a simple flow problem was modeled. The model simulated the injection of incompressible helium at a specified flow rate at the vessel inlet. The simulation was run in transient mode until the flow throughout the mesh achieved steady state. The flow was assumed to be laminar. A result of this calculation is shown in Figure 39. In order to visualize the flow, the y

component of gas velocity was plotted at the yz plane of symmetry. For visualization purposes the graphical output was mirrored across the z axis. The high speed inlet jet is clearly visible in the spherical vessel. Note the injection point is a location .0127 m into the spherical space. The rectangular area on the right represents the flow into the ambient space. Note the jet exits the annular tube and stagnates on the wall to the right before exiting at the subsonic opening at the upper and low boundaries of the ambient space. The flow results indicate that the mesh is continuous throughout its interior and that such a mesh is ready to be used for the more complex powder evacuation problem.

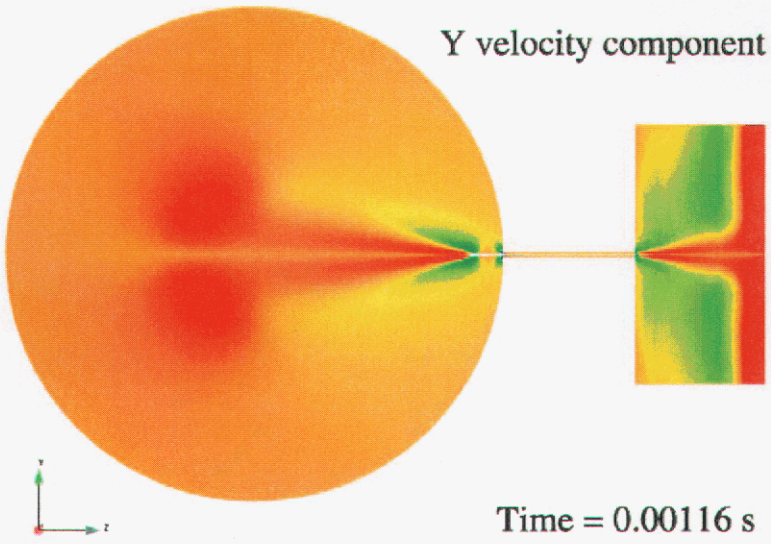

Figure 39. Incompressible helium flow through the computational mesh.

4. IMPROVED MODELS AND FUTURE WORK

Sandia's gas-powder modeling capability can be improved by addressing three important areas in FUEGO development. These are:

- Improvement of FUEGO compressible flow performance at high Mach numbers.
- Mass conservation of the solid phase.
- Improvements to the baseline gas-powder two-phase flow model

The need for improvements in compressible flow performance and conservation of the solid phase was discussed in the previous chapter. The remainder of this chapter will discuss baseline model improvements that can be made through the use of kinetic theory.

4.1. Maximum Solid Phase Volume Fraction Condition

There is a large degree of empiricism in the baseline gas-solid model described in Chapter 2. For example, the volume averaged equation for solid phase momentum, Equation (2.8), has terms for solid phase pressure and solid phase shear stress that must be modeled. The expression for solid phase pressure gradient, Equation (2.19), is designed to yield an increasing pressure gradient as the solid phase volume fraction increases, thus keeping the solid phase volume fraction from attaining unrealistically high values. We are interested in starting the powder evacuation problem from a condition of a stationary packed powder in a container where there is an interface between the packed powder and gas above. It may also be of interest to begin the simulation with the powder uniformly distributed throughout the container and then allow the powder to settle until the maximum solid phase volume fraction is achieved. Initial simulations with the baseline solid phase pressure model yielded numerical instabilities in particle settling problems. We have several ideas for modifying the baseline solid phase pressure gradient expression to avoid these problems including using less stiff expressions as the solid phase volume fraction approaches the maximum value and replacing the solid phase momentum equation with a constraint condition on the solid phase volume fraction.

4.2. Kinetic Theory Expressions for Solid Phase Pressure and Shear Stress

Recently efforts have been made (e.g., Gidaspow [10]) to reduce the amount of empiricism by applying the kinetic theory of dense gases (Chapman and Cowling [16]) to the problem of gas-solid flows. Specifically, the effects of particle-particle collisions have been addressed using kinetic theory to obtain expressions for solid phase pressure and solid phase shear stress that appear in the volume averaged equation for solid phase momentum. The concept of a granular temperature Θ arises where

$$\Theta = \frac{1}{3}\overline{v_s'^2} \tag{4.1}$$

and $\overline{v_s'^2}$ is the mean square of the solid phase velocity fluctuation. A transport equation for Θ can be derived and is given by

$$\frac{3}{2}\left[\frac{\partial}{\partial t}\left(\varepsilon_s\tilde{\rho}_s\Theta\right)+\nabla\cdot\left(\varepsilon_s\tilde{\rho}_s\vec{v}_s\Theta\right)\right]=\tilde{\vec{\tau}}_s:\nabla\vec{v}_s+\nabla\cdot\left(\kappa\nabla\Theta\right)-\gamma \tag{4.2}$$

where

$$\kappa=\frac{2\kappa_{\text{dilute}}}{\left(1+e\right)g_o}\left[1+\frac{6}{5}\left(1+e\right)g_o\varepsilon_s\right]^2+2{\varepsilon_s}^2\tilde{\rho}_s d_s\left(1+e\right)g_o\sqrt{\frac{\Theta}{\pi}} \tag{4.3}$$

$$\kappa_{\text{dilute}}=\frac{75\sqrt{\pi}}{384}\tilde{\rho}_s d_s\sqrt{\Theta} \tag{4.4}$$

and

$$\gamma=3\left(1-e^2\right){\varepsilon_s}^2\tilde{\rho}_s g_o\Theta\left[\frac{4}{d_s}\sqrt{\frac{\Theta}{\pi}}-\nabla\cdot\vec{v}_s\right] \quad . \tag{4.5}$$

The solid phase pressure is then given by

$$P_s=\varepsilon_s\tilde{\rho}_s\Theta\left[1+2\left(1+e\right)g_o\varepsilon_s-\left(0.73\varepsilon_s+8.957{\varepsilon_s}^2\right)\right] \tag{4.6}$$

and the solid phase stress tensor, solid phase bulk viscosity, and solid phase shear viscosity are given by

$$\tilde{\vec{\tau}}_s=\left(-P_s+\xi_s\nabla\cdot\vec{v}_s\right)\hat{I}+\tilde{\mu}_s\left\{\nabla\vec{v}_s+\nabla\vec{v}_s{}^T-\frac{2}{3}\nabla\cdot\vec{v}_s\hat{I}\right\} \tag{4.7}$$

$$\xi_s=\frac{4}{3}{\varepsilon_s}^2\tilde{\rho}_s d_s\left(1+e\right)g_o\sqrt{\frac{\Theta}{\pi}} \tag{4.8}$$

and

$$\tilde{\mu}_s=\frac{2\tilde{\mu}_{s,\text{dilute}}}{\left(1+e\right)g_o}\left[1+\frac{4}{5}\left(1+e\right)g_o\varepsilon_s\right]^2+\frac{4}{5}{\varepsilon_s}^2\tilde{\rho}_s d_s\left(1+e\right)g_o\sqrt{\frac{\Theta}{\pi}} \tag{4.9}$$

where

$$\tilde{\mu}_{s,\text{ dilute}}=\frac{5\sqrt{\pi}}{96}\tilde{\rho}_s d_s\sqrt{\Theta} \quad , \tag{4.10}$$

respectively. A parameter in the model is the coefficient of restitution, e, which accounts for energy dissipation due to non-ideal particle-particle collisions. The radial distribution function, g_o, which accounts for the statistics of spatial arrangement of particles is given by

$$g_o=\left[1-\left(\frac{\varepsilon_s}{\varepsilon_{s,\max}}\right)^{\frac{1}{3}}\right]^{-1} \quad . \tag{4.11}$$

A potential simplification of the above model is to neglect convection and diffusion of particle kinetic energy by assuming a local equilibrium between production and dissipation of particle kinetic energy which results in the following algebraic

equation for granular temperature

$$\tilde{\tilde{\tau}}_s : \nabla \vec{v}_s - \gamma = 0 \quad . \tag{4.12}$$

A similar analogy is often made in the statistical theory of turbulence for modeling the transport of turbulent kinetic energy and its dissipation rate in single phase fluid flow.

4.3. Turbulence Modeling

The influence of gas phase turbulence on solid phase momentum transport and vice versa is accounted for in the baseline model through turbulent dispersion terms in equations (2.7) and (2.8). More physically based turbulence modeling techniques have been proposed in the literature and require further study and implementation. This includes *e.g.*, the Tchen theory [17] of dispersion of particles by homogeneous turbulence where algebraic expressions are used to describe the solid phase turbulence in terms of the gas phase turbulence. Also, transport equations for the solid phase turbulent kinetic energy and dissipation rate (analogous to the gas phase *k-e* model) can be solved to describe the gas-solid turbulent transport.

This page intentionally blank

5. REFERENCES

[1] W.S. Winters, "TOPAZ – The Transient One-Dimensional Pipe Flow Analyzer: An Update on Code Improvements and Increased Capabilities," SAND87-8225, Sandia National Laboratories, Livermore, CA, September, 1987.

[2] E.W. Lemmon, A.P. Peskin, M.O. McLinden and D.G. Friend "NIST12 Thermodynamic and Transport Properties of Pure Fluids," http://www.nist.gov/srd/nist12.htm, N.I.S.T., 2000.

[3] W.S. Winters, "TOPAZ-The Transient One-Dimensional Pipe Flow Analyzer: Code Validation and Sample Problems," SAND85-8236, Sandia National Laboratories, Livermore, CA, February 1989.

[4] S. Crist, P.M. Sherman and R.R.Glass, "Study of the Highly Underexpanded Sonic Jet, AIAA Journal, Volume 4, Number 1, January, 1966.

[5] A.L. Addy "Effects of Axisymmetric Sonic Nozzle Geometry on Mach Disk Characteristics," AIAA Journal, Volume 19, Number 1, January 1981.

[6] A.H. Shapiro, The Dynamics and Thermodynamics of Compressible Fluid Flow, Volume I, John Wiley & Sons, New York, NY, 1953.

[7] A.D.B. Burns, Th. Frank, I. Hamil, and J-M. Shi, Drag Model for Turbulent Dispersion in Eulerian Multi-Phase Flows, 5th Int. Conf. on Multiphase Flow, ICMF-2004, Yokohama, Japan.

[8] CFX-5.7 Theory Manual.

[9] S. Ergun, Fluid Flow through Packed Columns, Chem. Eng. Prog., v. 48, 1952, pp. 89-94.

[10] D. Gidaspow, Multiphase Flow and Fluidization – Continuum and Kinetic Theory Descriptions, Academic Press, 1994.

[11] A. Neri and D. Gidaspow, Riser Hydrodynamics: Simulation using kinetic theory, AIChE J, v. 46, no. 1, January 2000, pp. 52-67.

[12] C.Y. Wen, and Y.H. Yu, Mechanics of Fluidization, Chem. Eng. Prog. Symp. Ser., v. 62, 1966, pp. 100-111.

[13] R.B. Bird, W.E. Stewart, E.N. Lightfoot, Transport Phenomena, John Wiley & Sons Inc., New York, N. Y. 1960.

[14] J. Bear, Dynamics of Fluids in Porous Media, American Elsevier Publishing Co., 1972.

[15] H. Moritomi, T. Iwase, and T. Chiba, A Comprehensive Interpretation of Solid Layer Inversion in Liquid Fluidised Beds, Chem. Eng. Sci., v. 37, no. 12, 1982, pp. 1751-1757.

[16] S. Chapman and T. G. Cowling, The Mathematical Theory of Non-uniform Gases, 2nd ed., Cambridge University Press, Cambridge, U. K. 1961.

[17] C. M. Tchen, Mean values and correlation problems connected with the motion of small particles suspended in a turbulent fluid, Doctoral dissertation, Delft, The Netherlands, 1947.

DISTRIBUTION

1 University of California
Attn: Professor Ralph Greif
Department of Mechanical Engineering
Berkeley, CA 94720

1	MS0139	P. Yarrington	01910
1	MS0382	S. P. Domino	01541
1	MS0382	S. E. Gianoulkis	01541
1	MS0427	S. E. Klenke	02118
1	MS9035	C. H. Cadden	08224
1	MS9035	S. F. Rice	08224
1	MS9035	W. R. Even	08220
1	MS9104	A. R. Ortega	08229
1	MS9153	G. A. Thomas	08240
1	MS9154	A. F. Baker	08224
1	MS9161	A. E. Pontau	08750
1	MS9292	M. D. Kanouff	08757
1	MS9404	D. M. Kwon	08770
5	MS9409	G. H. Evans	08757
1	MS9409	W. G. Houf	08757
1	MS9409	C. D. Moen	08757
1	MS9409	G. J. Wagner	08757
5	MS9409	W. S. Winters	08757
1	MS9661	P. Van Blarigan	08224
2	MS9018	Central Technical Files	08944
2	MS0899	Technical Library	04536